Noname manuscript No.
(will be inserted by the editor)

Climate change projections using the IPSL-CM5 Earth System Model: from CMIP3 to CMIP5

Dufresne J-L · Foujols, M-A · Denvil, S. · Caubel, A. · Marti, O. · Aumont, O · Balkanski, Y · Bekki, S · Bellenger, H · Benshila, R · Bony, S · Bopp, L · Braconnot, P · Brockmann, P · Cadule, P · Cheruy, F · Codron, F · Cozic, A · Cugnet, D · de Noblet, N · Duvel, J-P · Ethé, C · Fairhead, L · Fichefet, T · Flavoni, S · Friedlingstein, P · Grandpeix, J-Y · Guez, L · Guilyardi, E · Hauglustaine, D · Hourdin, F · Idelkadi, A · Ghattas, J · Joussaume, S · Kageyama, M · Krinner, G · Labetoulle, S · Lahellec, A · Lefebvre, M-P · Lefevre, F · Levy, C · Li, Z. X. · Lloyd, J · Lott, F · Madec, G · Mancip, M · Marchand, M · Masson, S · Meurdesoif, Y · Mignot, J · Musat, I · Parouty, S · Polcher, J · Rio, C · Schulz, M · Swingedouw, D · Szopa, S · Talandier, C · Terray, P · Viovy, N

Received: date / Accepted: date

J.-L. Dufresne
LMD/IPSL (Laboratoire de Météorologie Dynamique, Institut Pierre Simon Laplace), Paris, France
UMR 8539, Centre National de la Recherche Scientifique (CNRS), Ecole Normale Supérieur (ENS), Ecole Polytechnique (EP), Université Pierre et Marie Curie (UPMC)
UPMC Boite 99, 4 place Jussieu, 75752 Paris cedex 05, France
E-mail: Jean-Louis.Dufresne@lmd.jussieu.fr

Bony, S · Cheruy, F · Codron, F · Duvel, J-P · Fairhead, L · Grandpeix, J-Y · Guez, L · Hourdin, F · Idelkadi, A · Lahellec, A · Lefebvre, M-P · Li, Z. X. · Lott, F · Musat, I · Polcher, J · Rio, C
LMD/IPSL (Laboratoire de Météorologie Dynamique, Institut Pierre Simon Laplace), Paris, France
UMR 8539, Centre National de la Recherche Scientifique (CNRS), Ecole Normale Supérieur (ENS), Ecole Polytechnique (EP), Université Pierre et Marie Curie (UPMC)

Cadule, P · Denvil, S. · Ethé, C · Foujols, M-A · Ghattas, J · Mancip, M
IPSL (Institut Pierre Simon Laplace), Paris, France
FR 636, Centre National de la Recherche Scientifique (CNRS), Université de Versailles Saint-Quentin (UVSQ), Université Pierre et Marie Curie (UPMC), Commissariat à l'Energie Atomique (CEA), Institut de Recherche pour le Développement (IRD), Ecole Normale Supérieure (ENS), Ecole Polytechnique, Université Denis Diderot, Université Paris-Est Créteil

Balkanski, Y · Bopp, L · Braconnot, P · Brockmann, P · Caubel, A. · Cozic, A · de Noblet, N · Friedlingstein, P · Hauglustaine, D · Joussaume, S · Kageyama, M · Marti, O. · Meurdesoif, Y · Schulz, M · Swingedouw, D · Szopa, S · Viovy, N
LSCE/IPSL (Laboratoire des Sciences du Climat et de l'Environnement, Institut Pierre Simon Laplace)), Gif-sur-Yvette, France
UMR 8212, Centre National de la Recherche Scientifique (CNRS), Commissariat à l'Energie Atomique (CEA), Université de Versailles Saint-Quentin (UVSQ)

Bekki, S · Cugnet, D · Lefevre, F · Marchand, M
LATMOS/IPSL (Laboratoire Atmosphères, Milieux, Observations Spatiales, Institut Pierre Simon Laplace)), Paris, France
UMR 8190, Centre National de la Recherche Scientifique (CNRS), l'Université de Versailles Saint-Quentin (UVSQ), Université Pierre et Marie Curie (UPMC)

Bellenger, H · Benshila, R · Flavoni, S · Guilyardi, E · Labetoulle, S · Levy, C · Lloyd, J · Madec, G · Masson, S · Mignot, J · Talandier, C · Terray, P
LOCEAN/IPSL (Laboratoire d'Océanographie et du Climat : Expérimentation et Approches Numériques, Institut Pierre Simon Laplace), Paris, France
UMR 7159, Centre National de la Recherche Scientifique (CNRS), Université Pierre et Marie Curie (UPMC), Institut de Recherche pour le Développement (IRD), Museum National d'Histoire Naturelle (MNHM)

Krinner, G · Parouty, S
LGGE (Laboratoire de Glaciologie et Géophysique de l'Environnement), Grenoble, France
UMR 5183, Centre National de la Recherche Scientifique (CNRS), Université Joseph Fourier (UJF)

Abstract We present here the global general circulation model IPSL-CM5 developed to study the long-term response of the climate system to natural and anthropogenic forcings as part of the 5th Phase of the Coupled Model Intercomparison Project (CMIP5). This model includes an interactive carbon cycle, a representation of tropospheric and stratospheric chemistry, and a comprehensive description of aerosols. As it represents the principal dynamical, physical and bio-geochemical processes of relevance in the climate system, it may be referred to as an Earth System Model. However, IPSL-CM5 may be used in a multitude of configurations associated with different boundary conditions and with a range of complexities in terms of processes and interactions. This paper presents an overview of the different model components, and explains how they were coupled/used to simulate historical climate changes over the past 150 years and different scenarios of future climate change.

A single version of the IPSL-CM5 model (IPSL-CM5A-LR) was used to provide climate projections associated with different socio-economic scenarios, including the different Representative Concentration Pathways (RCPs) considered by CMIP5, and several Scenarios from the Special Report on Emission Scenarios (SRES) considered by CMIP3. Results suggest that the magnitude of global warming projections primarily depends on the socio-economic scenario considered, that there is potential for an agressive mitigation policy to limit global warming to about two degrees, and that the behaviour of some components of the climate system such as the Arctic sea ice and the Atlantic Meridional Overturning Circulation may change drastically by the end of the 21st century in the case of a no climate policy scenario. Although the magnitude of regional temperature and precipitation changes depends fairly linearily on the magnitude of the projected global warming (and thus on the scenario considered), the geographical pattern of these changes turns out to be strikingly similar for the different scenarios. The representation of atmospheric physical processes in the model is shown to have a strong influence on the simulated climate variability and on both the magnitude and the pattern of the projected climate changes.

1 Introduction

As climate change projections rely on climate model results, the scientific community regularly organize international projects to intercompare these models. Over the years, the various phases of the Coupled Model Intercomparison Project (CMIP) have regularly grown both in terms of number of participants and in terms of scientific impacts. The model outputs made available by the third phase (CMIP3, Meehl et al., 2005, 2007a) lead to hundreds of publications and provided important inputs to the IPCC fourth assessment report (IPCC, 2007). The fifth phase, CMIP5 (Taylor et al., 2011), is also expected to serve the scientific community for many years and to provide major inputs to the forthcoming IPCC fifth assessment report.

The IPSL-CM4 model (Marti et al., 2010), developed at Institut Pierre Simon Laplace (IPSL) is one of the models that contributed to CMIP3. It is a classical climate model that couples an atmosphere-land surface model to a ocean-sea ice model. It has been used to simulate and to analyze tropical climate variability (Braconnot et al., 2007), climate changes projections (Dufresne et al., 2005), the impact of Greenland ice sheet melting on the Atlantic meridional overturning circulation (Swingedouw et al., 2007b), among other studies. Using the same "physical package", separate developments have been carried out to simulate tropospheric chemistry (Hauglustaine et al., 2004), tropospheric aerosols (Balkanski et al., 2010), stratospheric chemistry (Jourdain et al., 2008) and the carbon cycle (Friedlingstein et al., 2006; Cadule et al., 2009). This latter model has been used to study feedbacks between climate and biogeochemical processes. For instance, Lenton et al. (2009) have shown that a change in stratospheric ozone may modify the carbon cycle through a modification of the atmospheric and oceanic circulation. Lengaigne et al. (2009) have suggested positive feedbacks between the sea-ice extent and chlorophyll distribution in the Arctic region at the seasonal time scale.

The IPSL-CM5 model, which is presented here, is an Earth System Model (ESM) that includes all the previous developments and which contributes to CMIP5. More than a single model, it is a platform that allows a consistent suite of models with various degrees of complexity, various numbers of components and processes, and different resolutions. This flexibility is difficult to implement and to maintain, but is useful for many studies. For instance, when studying the various feedbacks of the climate system, it is common to replace some components or processes by prescribed conditions.

Aumont, O
LPO (Laboratoire de Physique des Océans), Brest, France
UMR 6523, Centre National de la Recherche Scientifique (CNRS), Institut français de recherche pour l'exploitation de la mer (Ifremer), Institut de Recherche pour le Développement (IRD), Université de Bretagne Occidentale (UBO)

Fichefet, T
Georges Lemaître Centre for Earth and Climate Research, Earth and Life Institute, Université catholique de Louvain, B-1348 Louvain-la-Neuve, Belgium.

For the atmosphere, when evaluating the performance of the aerosol and chemistry components, one may want to nudge the global atmospheric circulation to the observed one. For more theoretical studies or to examine the robustness of some climate features, one may wish to drastically simplify the system by simulating for instance an idealized aqua-planet.

It is also interesting to have different version of a model with different "physical packages", i.e. different sets of consistent parameterizations. First, it allows us to make some dedicated studies of the climate system (e.g. Braconnot et al., 2007). Second, it facilitates the developments of the ESM, which is a permanent ongoing process. Indeed, developing and adjusting the physical package requires time. As these developments have a strong impact on the characteristics of the biogeochemistry variables (aerosol concentration, chemistry composition, etc...), it is important that a frozen version of the physical package is used while the models including the other processes are in development. In the previous IPSL-CM4 model, most of the chemistry and aerosol studies where first made using the LMDZ atmospheric model with the Tiedke convective scheme (Tiedtke, 1989) while the Emanuel convective scheme (Emanuel, 1991) was included and developed to improve the characteristics of the simulated climate. However these two versions were not included in a single framework and have diverged over the years. Conversely, the new IPSL model includes two physical packages within the same framework. IPSL-CM5A is an extension of IPSL-CM4 with an improved ocean model and is now used as an ESM. IPSL-CM5B includes an improved set of physical parameterization of the atmospheric model (Hourdin et al., this issue-b).

The outline of the paper is the following.The IPSL-CM5 model and its various components are briefly presented in section 2. The different model configurations and the different forcings used to performed the CMIP5 long-term experiments are presented in section 3. Among these experiments, climate change simulations of the twentieth century and projections for the twenty-first century are analyzed in section 4 and 5. Then we analyze for different versions of the IPSL model the climate variability and the climate response to the same forcing (section 6). Summary and conclusions are given in section 7.

2 The IPSL-CM5 model and its components

2.1 The platform

The IPSL-CM5 ESM platform allows a large range of model configurations which aim to address different scientific questions. These configurations may differ in various ways: physical parametrization, horizontal resolution, vertical resolution, number of components (atmosphere and land surface only, ocean and sea ice only, coupled atmosphere - land surface - ocean - sea ice) and number of processes (physical, chemistry, aerosols, carbon cycle) (Fig. 1).

The IPSL-CM5 model is built around a physical core that includes atmosphere, land-surface, ocean and sea-ice components. It also includes biogeochemical processes through different models: stratospheric and tropospheric chemistry, aerosols, terrestrial and oceanic carbon cycle (Fig. 1-a). To test specific hypothesis or feedback mechanisms, components of the model may be suppressed and replaced by prescribed boundary conditions or values (section 3). In the next sub-sections, we will give a general overview of the various models included in the IPSL-CM5 model.

[Fig. 1 about here.]

2.2 Atmosphere

2.2.1 Atmospheric GCM: LMDZ5A and LMDZ5B

LMDZ is an atmospheric general circulation model developed at the Laboratoire de Météorologie Dynamique. The dynamical part of the code is based on a finite-difference formulation of the primitive equations of meteorology (Sadourny and Laval, 1984) on a staggered and stretchable (the Z of LMDZ standing for Zoom) longitude-latitude grid. Vapor, liquid water and atmospheric trace species are advected with a monotonic second order finite volume scheme (Van Leer, 1977; Hourdin and Armengaud, 1999). On the vertical, the model uses a classical so-called hybrid $\sigma - p$ coordinate. With respect to the previous LMDZ4 version, the number of layers has been increased from 19 to 39, with 15 levels above 20 km. The L39 discretization goes up to about the same altitude as the stratospheric LMDZ4-L50 version (Lott et al., 2005) and is fine enough to resolve the propagation of the mid-latitude waves in the stratosphere and to produce sudden-stratospheric warming. Two versions of LMDZ5 can be used within IPSL-CM5 that differ by the parameterization of turbulence, convection and clouds.

In the LMDZ5A version, (Hourdin et al., this issue-a) the physical parametrization are very close to that of the previous LMDZ4 version used for CMIP3 (Hourdin et al., 2006). The radiation scheme is inherited from the European Center for Medium-Range Weather Forecasts (Fouquart and Bonnel, 1980; Morcrette et al., 1986). The dynamical effects of the subgrid-scale orography are parametrized according to Lott (1999). Turbulent transport in the planetary boundary layer is treated as a vertical eddy diffusion (Laval et al., 1981) with counter-gradient correction and dry convective adjustment. The surface boundary layer is treated according to Louis (1979). Cloud cover and cloud water content are computed using a statistical scheme (Bony and Emanuel, 2001). For deep convection, the LMDZ5A version uses the "episodic mixing and buoyancy sorting" scheme originally developed by Emanuel (1991). LMDZ5A is used within the IPSL-CM5A model.

In the "New Physics" LMDZ5B version, (Hourdin et al., this issue-b) the representation of the boundary layer is ensured by an eddy-diffusion combined with a "thermal plume model" to represent the coherent structures of the convective boundary layer (Hourdin et al., 2002; Rio and Hourdin, 2008; Rio et al., 2010). The cloud scheme is coupled to both the convection scheme (Bony and Emanuel, 2001) and the boundary layer scheme (Jam et al., 2011) assuming that the subgrid scale distribution of total water can be represented by a generalized log-normal distribution in the first case, and by a bi-Gaussian distribution in the second case. In both cases, the statistical moments of the total water distribution are diagnosed as a function of both large-scale environmental variables and of subgrid scale variables predicted by the convection or turbulence parameterizations. The triggering and the closure of the Emanuel (1991) convective scheme have been modified and are now based on the notions of Available Lifting Energy (ALE) for the triggering and Available Lifting Power (ALP) for the closure. A parameterization of the cold pools generated by the re-evaporation of convective rainfall has been introduced (Grandpeix and Lafore, 2010; Grandpeix et al., 2010). The LMDZ5B version is characterized by a much better representation of the boundary layer and associated clouds, by a shift of the diurnal cycle of continental convection by several hours and a stronger and more realistic tropical variability. LMDZ5B is used within the IPSL-CM5B model.

2.2.2 Stratospheric chemistry: REPROBUS

The REPROBUS (Reactive Processes Ruling the Ozone Budget in the Stratosphere) module (Lefevre et al., 1994, 1998) coupled to a tracer transport scheme is used to calculate interactively the global distribution of trace gases, aerosols and clouds within the stratosphere in the LMDZ atmospheric model. The module is extensively described in Jourdain et al. (2008). It includes 55 chemical species and the associated stratospheric gas-phase and heterogeneous chemical reactions. Absorption cross-sections and kinetics data are based on the latest JPL recommendations (Sander et al., 2006). The photolysis rates are calculated off-line using a look-up table generated with the Tropospheric and Ultraviolet visible (TUV) radiative model (Madronich and Flocke, 1998). The heterogeneous chemistry component takes into account the reactions on sulfuric acid aerosols, and liquid (ternary solution) and solid (NAT, ice) Polar Stratospheric Clouds (PSCs). The gravitational sedimentation of PSCs is also simulated.

2.2.3 Tropospheric chemistry and aerosol: INCA

The INteraction with Chemistry and Aerosol (INCA) model simulates the distribution of aerosols and gaseous reactive species in the troposphere. The model accounts for surface and in-situ (lightning, aircraft) emissions, scavenging processes and chemical transformations. LMDZ-INCA simulations are performed with an horizontal grid of 3.75 degrees in longitude and 1.9 degrees in latitude (96x95 grid points). The vertical grid is still based on the former LMDZ4 19 levels. Fundamentals for the gas phase chemistry are presented in Hauglustaine et al. (2004); Folberth et al. (2006). The tropospheric photochemistry is described through a total of 117 tracers including 22 tracers to represent aerosols and 82 reactive chemical tracers to represent tropospheric chemistry. The model includes 223 homogeneous chemical reactions, 43 photolytic reactions and 6 heterogeneous reactions including non-methane hydrocarbon oxidation pathways and aerosol formation. Biogenic surface emissions of organic compounds and soil emissions are provided from off-line simulations with the ORCHIDEE land surface model as described by Lathière et al. (2005). In this tropospheric model, ozone concentrations are relaxed toward present-day observations at the uppermost model levels (altitudes higher than the 380K potential temperature level). The changes in stratospheric ozone from pre-ozone hole conditions to the future are therefore not accounted for in the simulations.

For aerosols, the INCA module simulates the distribution of anthropogenic aerosols such as sulfates, black carbon (BC), particulate organic matter (POM), as well as natural aerosols such as sea-salt and dust. The aerosol code keeps track of both the number and the mass of aerosols using a modal approach to treat the size distribution, which is described by a superposition of log-normal modes (Schulz et al., 1998). Three size modes are considered: a sub-micronic (diameters less than 1 μm), a micronic (diameters between 1 and 10 μm) and a super-micronic (diameters >10 μm). To account for the diversity in chemical composition, hygroscopicity and mixing state, we distinguish between soluble and insoluble modes. Sea-salt, SO_4, and methane sulfonic acid (MSA), are treated as soluble components of the aerosol, dust is treated as insoluble species, whereas, black carbon (BC) and particulate organic matter appear both in the soluble or insoluble fractions. The aging of primary insoluble carbonaceous particles transfers insoluble aerosol number and mass to soluble with a half-life time of 1.1 days. Details on the aerosol component of INCA can be found in Schulz (2007); Balkanski (2011).

The INCA model setup used to generate the aerosols and tropospheric ozone fields used in these CMIP5 simulations as well as the associated radiative forcings are described in details by Szopa et al. (this issue) (see also sections 3.5 and 3.7).

2.2.4 Coupling between chemistry, aerosol and atmospheric circulation

The radiative impact of dust, sea salt, black carbon and organic carbon aerosols was introduced in LMDZ as described in Déandreis (2008) and Balkanski (2011). The growth in aerosol size with increased relative humidity is computed using the method described by Schulz (2007). The effect of aerosol on cloud droplet radius without affecting cloud liquid water content (the so-called first indirect effect) is also considered. To parametrize this effect, the cloud droplet number concentration is computed from the total mass of soluble aerosol through the prognostic equation from Boucher and Lohmann (1995). The coefficient were taken from aerosol-cloud relationships derived from Polder satellite measurements (Quaas and Boucher, 2005). Both direct and first indirect aerosol radiative forcings are estimated through multiple calls to the radiative code.

The tropospheric chemistry and aerosols may be either computed or prescribed. When computed, the INCA and LMDZ models are coupled at each time step to account for interactions between chemistry, aerosol and climate. Otherwise, the aerosol concentration is usually prescribed with monthly mean values linearly interpolated for each day. Déandreis et al. (2011) have analyzed in detail the difference in results obtained with on-line and off-line setup. They showed that the differences were generally small, that the radiative forcings was very difficult to estimate with the on-line simulation and they propose some solutions with different levels of accuracy and complexity.

Similarly, the stratospheric chemistry and, in particular, ozone may be either computed or prescribed. When computed, the REPROBUS and LMDZ models are coupled at each time step to account for chemistry-climate interactions. When prescribed, LMDZ is forced by day-time and night-time ozone concentrations above the mid-stratosphere whereas it is forced by daily mean ozone fields below. Indeed, ozone concentration exhibit a strong diurnal cycle in the upper stratosphere and mesosphere. Neglecting these diurnal variations leads to an overestimate of the infra-red radiative cooling and therefore to a cold bias of the atmosphere.

2.3 Land surface model: ORCHIDEE

ORCHIDEE (ORganizing Carbon and Hydrology In Dynamic EcosystEms) is a land-surface model that simulates the energy and water cycles of soil and vegetation, the terrestrial carbon cycle, and the vegetation composition and distribution (Krinner et al., 2005). The land surface is described as a mosaic of twelve plant functional types (PFTs) and bare soil. The definition of PFT is based on ecological parameters such as plant physiognomy (tree or grass), leaves (needleleaf or broadleaf), phenology (evergreen, summergreen or raingreen) and photosynthesis type for crops and grasses (C3 or C4). Relevant biophysical and biogeochemical parameters are prescribed for each PFT.

ORCHIDEE is based on three different modules. The first module, called SECHIBA (Ducoudré et al., 1993; de Rosnay and Polcher, 1998), describes the exchanges of energy and water between the atmosphere and the biosphere, and the soil water budget. It also includes a routing module which transports through rivers and aquifers the water which is not infiltrated or drained at the bottom of the soil (d'Orgeval et al., 2008). The tight integration of the routing allows to re-evaporate the water on its way to the ocean through processes such as floodplains or irrigation (de Rosnay et al., 2003). When coupled with LMDZ, both models have the same spatial resolution and time step. The coupling procedure for the heat and water fluxes uses an implicit approach as described in Marti et al. (2010).

The second module, STOMATE (Saclay Toulouse Orsay Model for the Analysis of Terrestrial Ecosystems), represents the phenology and carbon dynamics of the terrestrial biosphere (Krinner et al., 2005). STOMATE simulates, with a daily time step, processes as photosynthesis, carbon allocation, litter decomposition, soil carbon dynamics, maintenance and growth respiration, and phenology. Plant assimilation is based on Farquhar et al. (1980) for C3 plants and on Collatz et al. (1992) for C4 plants. Maintenance respiration is a function of each living biomass pool and temperature, while growth respiration is computed as a fraction of the difference between assimilation inputs and maintenance respiration outputs to plant biomass.

Finally, the third module, based on the global LPJ (Lund-Potsdam-Jena) vegetation model (Sitch et al., 2003), represents long-term processes (yearly time step) and simulates vegetation dynamics, fire, sapling establishment, light competition, and tree mortality. The PFT distribution can be either prescribed from an input inventory (static mode, LPJ deactivated), or entirely simulated by the model depending on climate conditions (dynamic mode, LPJ activated). The fraction of grid space covered by agricultural croplands is always prescribed, so that crop extent is not affected by dynamic vegetation change. The PFT distribution is prescribed in the simulations presented in this article.

2.4 Ocean and sea-ice

The ocean and sea-ice component is based on NEMOv3.2 (Nucleus for European Modelling of the Ocean, Madec, 2008), which includes OPA for the dynamics of the ocean, PISCES for ocean biochemistry, and LIM for sea-ice dynamics and thermodynamics. The configuration is ORCA2 (Madec and Imbard, 1996): south of 40°N, the grid is an isotropic Mercator with a nominal resolution of 2°. A latitudinal grid refinement of 1/2° is used in the tropics. North of 40°N, the grid is non geographic and quasi-isotropic. The North Pole singularity is replaced by a line between points in Canada and Siberia. In the vertical, 31 levels are used (from 10m near the surface to 500m at 5000m).

2.4.1 Oceanic GCM: NEMO

NEMOv3.2 takes advantage of several improvements over OPA8.2, the ocean model version used in IPSL-CM4. It uses a partial step formulation (Barnier et al., 2006), which ensures a better representation of bottom bathymetry and thus stream flow and friction at the bottom of the ocean. Advection of temperature and salinity is done using a total variance dissipation scheme (Lévy et al., 2001; Cravatte et al., 2007). In the momentum equation, an energy and enstrophy conserving scheme is used (Arakawa and Lamb, 1981; Le Sommer et al., 2009). The mixed layer dynamics is parameterized using the Turbulent Kinetic Energy (TKE) closure scheme of Blanke and Delecluse (1993) improved by Madec (2008). The improvements include a double diffusion process (Merryfield et al., 1999), Langmuir cells (Axell, 2002) and the contribution of surface wave breaking (Mellor and Blumberg, 2004; Burchard and Rennau, 2008). A parametrization of bottom intensified tidal-driven mixing similar to Simmons et al. (2004) is used in combination with a specific tidal mixing parametrization in the Indonesian area (Koch-Larrouy et al., 2007, 2010). Besides, NEMOv3.2 includes prognostic interaction between incoming shortwave radiation into the ocean and the phytoplankton (Lengaigne et al., 2009).

The horizontal eddy viscosity coefficient (ahm) value is 4.10^4 $m^2.s^{-1}$ and the lateral eddy diffusivity coefficient (aht) value is 10^3 $m^2.s^{-1}$. ahm reduces to aht in the tropics, except along western boundaries. The tracer diffusion is along isoneutral surfaces. A Gent and Mcwilliams (1990) term is applied in the advective formulation. Its coefficient is calculated from the local growth rate of baroclinic instability. It decreases in the 20°S-20°N band, and vanishes at the Equator. At the ocean floor, there is a linear bottom friction with a coefficient of 4.10^{-4}, and a background bottom turbulent kinetic energy of 2.5 10^{-3} $m^2.s^{-2}$. The model has a Beckmann and Döscher (1997) diffusive bottom boundary layer scheme with a value of 10^4 $m^2.s^{-1}$. A spatially varying geothermal flux is applied at the bottom of the ocean (Emile-Geay and Madec, 2009), with a global mean value of 86.4 $mW.m^{-2}$.

2.4.2 Sea ice : LIM2

LIM2 (Louvain-la-Neuve Sea Ice Model, Version 2) is a two-level thermodynamic-dynamic sea ice model (Fichefet and Morales Maqueda, 1997, 1999). Sensible heat storage and vertical heat conduction within snow and ice are determined by a three-layer model. The storage of latent heat inside the ice resulting from the trapping of shortwave radiation by brine pockets is taken into account. The surface albedo is parametrized as a function of the surface temperature and the snow and ice thicknesses. Vertical and lateral growth/decay rates of the ice are obtained from prognostic energy budgets at both the bottom and surface boundaries of the snow-ice cover and in leads. For the momentum balance, sea ice is considered as a two-dimensional continuum in dynamical interaction with atmosphere and ocean. The viscous-plastic constitutive law proposed by Hibler (1979) is used for computing the internal ice force. The ice strength is taken as a function of the ice thickness and compactness. The physical fields that are advected are the ice concentration, the snow and ice volume and enthalpy, and the brine reservoir. The sea ice and ocean models have the same horizontal grid.

2.4.3 Ocean carbon cycle: PISCES

PISCES (Pelagic Interaction Scheme for Carbon and Ecosystem Studies) (Aumont and Bopp, 2006) simulates the cycling of carbon, oxygen, and of the major nutrients determining phytoplankton growth (phosphate, nitrate, ammonium, iron and silicic acid). The carbon chemistry of the model is based on the Ocean Carbon Model Intercomparison Project (OCMIP2) protocol (Najjar et al., 2007) and the parametrization proposed by Wanninkhof (1992) is used to compute air-sea gas exchange of $\mathrm{CO_2}$ and O_2.

PISCES includes a simple representation of the marine ecosystem with two phytoplankton size classes, representing nanophytoplankton and diatoms, as well as two zooplankton size classes, representing microzooplankton and mesozooplankton. Phytoplankton growth is limited by the availability of nutrients, temperature, and light. There are three non-living components of organic carbon in the model: semi-labile dissolved organic carbon (DOC), with a lifetime of several weeks to years, as well as large and small detrital particles, which are fuelled by mortality, aggregation, fecal pellet production and grazing. Biogenic silica and calcite particles are also included.

Nutrients and/or carbon are supplied to the ocean from three different sources: atmospheric deposition, rivers and sediment mobilization. These sources are explicitly included but do not vary in time apart from a climatological seasonal cycle for the atmospheric input. Atmospheric deposition (Fe, N, P and Si) has been estimated from the INCA model (Aumont et al., 2008). River discharge of carbon and nutrients is taken from Ludwig et al. (1996). Iron input from sediment mobilization has been parameterized as in Aumont and Bopp (2006).

PISCES is used here not only to compute air-sea fluxes of carbon, but also to compute the effect of a biophysical coupling: the chlorophyll concentration produced by the biological component retroacts on the ocean heat budget by modulating the absorption of light as well as the oceanic heating rate (see Lengaigne et al. (2007) for a detailed description).

2.4.4 Atmosphere-Ocean-Sea ice coupling

The Atmosphere / Ocean / Sea ice coupling in IPSL-CM5 is very closed, with some improvements, to the coupling used in IPSL-CM4 and that has been presented in details in Marti et al. (2010). The atmospheric model has a fractional land-sea mask, each grid box being divided into four sub-surfaces corresponding to land surface, free ocean, sea ice and glaciers. The OASIS coupler (Valcke, 2006) is used to interpolate and exchange the variables and to synchronize the models. As a comprehensive model of glacier and land-ice is not yet included, the local snow mass is limited to $3,000\mathrm{kg.m}^2$ to avoid infinite accumulation, and the snow mass above this limit is sent as calving to the ocean. The coupling and the interpolation procedure ensure local conservation of energy and water, avoiding the need of any transformation to conserve these global quantities. Compared to Marti et al. (2010), the daily mean speed of the ocean surface is now sent to the atmosphere and used as boundary conditions for the atmospheric boundary layer scheme.

3 Experiments, model configurations and forcings for CMIP5

3.1 The CMIP5 experimental protocol

The CMIP5 project (Taylor et al., 2011) has been designed to address a much wider range of scientific questions than CMIP3 (Meehl et al., 2005), requiring a wider spectrum of models, configurations and experiments. CMIP5 includes experiments focussing on short and long time scales. However, only the long-term experiments will be considered in this paper. They include the few-hundred centuries long pre-industrial control simulation, the historical simulations (1850-2005) and the future projections simulations (2006-2100, 2006-2300). The future projections are performed under the new scenarios proposed by CMIP5, the so-called RCP (Representative Concentration Pathway) scenarios (Moss et al., 2010; van Vuuren et al., 2011), and labeled according to the approximate value of the radiative forcing (in Wm^{-2}) at the end of the 21st century: RCP-2.6, RCP-4.5, RCP-6 and RCP-8.5. On top of these, CMIP5 has also planned simulations with idealized forcings (1%/year $\mathrm{CO_2}$ increase, 4 times $\mathrm{CO_2}$ abrupt increase), forcings corresponding to prescribed or idealized sea-surface conditions (e.g. AMIP, aqua-planet), forcings representative of specific paleo-climate periods, and others. The total length of all these simulations exceeds a few thousands of years. This of course calls for optimizations and compromises between the available computer time and the simulations' degrees of complexity. The general strategy we have adopted consists in running the atmospheric component of the ESM at a rather low resolution, and to treat some of the atmospheric chemistry and transport processes controlling the greenhouse gases and the aerosols outside the ESM in a semi-offline way.

3.2 Model horizontal resolution

A systematic exploration of the impact of the atmospheric grid configuration on the simulated climate was conducted with IPSL-CM4 by (Hourdin et al., this issue-a). As the objective of this paper was to prepare CMIP5, rather coarse resolutions were explored. They found that the grid refinement has a strong impact on the jet locations, and on the pronounced mid latitude cold bias which was one of the major deficiencies of the IPSL-CM4 model. The impact of grid refinement on the jets location was also studied by Guemas and Codron (2011), who found that this location was controlled by the large scale atmospheric dynamics. They also found that the associated errors could be reduced at a moderate computational cost by increasing the resolution in latitude more than in longitude. Based on the findings of these studies, we finally retained for CMIP5 two grids based on almost the same number of points in longitude and latitude, so that the meshes are isotropic ($\delta x = \delta y$) at latitude 60^o and $\delta x = 2\delta y$ at the equator. At Low Resolution (LR), the model has 96×95 points corresponding to a resolution of $1.875^o \times 3.75^o$ and at Medium Resolution (MR) the model has 144×143 points, corresponding to a resolution of of $1.25^o \times 2.5^o$.

3.3 Ozone Concentrations

Interannual ozone variations are considered in the IPSL-CM5 simulations for CMIP5, which was not the case in the IPSL-CM4 simulations for CMIP3 where the model was only forced with a constant seasonally-varying ozone field. Nevertheless this inter annually varying ozone can not be routinely computed on-line using the very comprehensive aerosols and chemistry coupled models (section 2.2.2 and 2.2.3) in the IPSL ESM because they are very demanding in computer time. Actually, LMDZ-INCA and LMDZ-REPROBUS both need a few tens (50 to 100) of tracers, and running these models increases the CPU time by more than a factor of 10 compared to the atmospheric model LMDZ alone.

To circumvent this difficulty we assume that the short-term variations in ozone, even caused initially by short-term climate variability, play a relatively small, possibly negligible, role in the long-term evolution of climate. This assumption has been shown to be valid for stratospheric ozone (e.g. Son et al., 2010). On long time scales, stratospheric ozone is mostly influenced by climate change via stratospheric cooling due to CO_2 increase, and tropospheric ozone is influenced by changes in global mean temperature via the water vapor concentration. These effects of climate on ozone are accounted for in chemistry climate models run with prescribed SST (Fig. 1-b). In turn, the evolution of climate depends on the long-term changes in the concentration of ozone. This enables us to simplify the treatment of the two-way interactions between ozone and climate by decoupling them using a semi offline approach instead of the fully coupled online approach.

This approach is fully described in Szopa et al. (this issue) and consists of specifying in the ESM the ozone fields predicted by dedicated atmospheric chemistry coupled model simulations. To do so, two different atmospheric chemistry models were used. Since RCP climate model simulations were not yet available, the sea surface temperature and sea ice concentration prescribed in the chemistry simulations are taken from existing historical and scenario runs performed with the IPSL-CM4 model. We use SST of SRES-A2 scenario for the RCP8.5 simulation, SRES-A1B for RCP6.0, SRES-B1 for RCP4.5 and scenario E1 (Johns et al., 2011) for RCP2.6. The differences between the prescribed SST and those obtained with the RCP scenarios are not expected to strongly impact the atmospheric chemistry. First, the LMDZ-INCA model (section 2.2.3) with 19 vertical levels has been used to generate time-varying 3D fields of ozone in the troposphere. The simulations include decadal emissions of methane, carbon monoxide, nitrogen oxides and non methane hydrocarbons for anthropogenic and biomass burning emissions. They are taken from Lamarque et al. (2010) for the historical period and from Lamarque et al. (2011) for the RCP scenarios. Also, the monthly biogenic emissions are from Lathière et al. (2005) and are kept constant over the period. Second, the LMDZ-REPROBUS model (section 2.2.2) with 50 vertical levels is used to generate time-varying 3D fields of ozone in the stratosphere. Instead of running all the scenarios, time-varying ozone fields for some of the RCP scenarios are reconstructed by interpolating or extrapolating linearly from the CCMVal REF-B2 and SCN-B2c scenarios (Morgenstern et al., 2010) using a time-varying weighing coefficient proportional to the CO_2 level. This approach is based on the somewhat linear dependency of stratospheric ozone changes on CO_2 changes which has been found in coupled chemistry models run under the RCP scenarios (Eyring et al., 2010b,a). The INCA (tropospheric) and REPROBUS (stratospheric) ozone fields are then merged with a transition region centered on the tropopause region and averaged over longitudes to produce time-varying zonally-averaged monthly-mean ozone fields. For completeness, note also that the INCA and REPROBUS ozone fields have been extensively validated against a range of observation for the recent past period. For the future period, stratospheric projections have also been found to be in line with the ozone projections from well-established chemistry-climate models (i.e. SPARC, 2010; WMO, 2011).

3.4 Aerosol Concentrations

For CMIP5, the radiative impact of dust, sea salt, black carbon and organic carbon aerosols are introduced in LMDZ following Déandreis (2008) and Balkanski (2011). Again this is a substantial progress when compared to the IPSL-CM4 model for CMIP3, where only the sulfate aerosols were considered (Dufresne et al., 2005).

As for the ozone, aerosol microphysics strongly depends on weather and climate. However, there is no strong evidence that short-term variations in aerosol concentration play a significant role in the long-term evolution of climate. This enables us again to simplify the treatment of the coupling between aerosols and climate by using a semi offline approach. For the aerosols, this approach is supported by Déandreis et al. (2011), who made a careful comparison between on-line and off-line runs in the case of sulfate aerosols. They found little differences in the model results between the two approaches. We should nevertheless keep in mind that, for dust aerosols, the short term variations probably impact individual meteorological events, an effect that should be tested in a fully coupled environment.

The past and future evolutions of aerosol distribution are computed using the LMDZ-INCA model (section 2.2.3). Anthropogenic and biomass burning emissions are those provided by Lamarque et al. (2010) for the historical period and by Lamarque et al. (2011) for the RCP scenarios for the future. Since the IPSL-CM5 model has biases in surface winds, the natural emissions of dust and sea salt are computed using the 10m wind components provided by ECMWF for 2006 and, consequently, have seasonal cycles but no inter-annual variations. The computed monthly mean aerosol fields are then smoothed with an 11 years running mean. The methodology to build the aerosol field as well as their evolution and realism are described in a more detailed manner in Szopa et al. (this issue). In the first release of these climatologies (used for the IPSL-CM5A-LR simulations), the particulate organic matter computation was underestimated by almost 20%. This induces a slight underestimation of the aerosol cooling effect, but additional simulations show it has very little impact on climate. A common deficiency with the low and medium resolution is that there is no coupling between dust and sea-salt emissions, and climate via the surface winds. Nonetheless, the couplings via the transport and the wet and dry deposition and the forcing via land-use changes are still described in the model.

3.5 CO_2 concentrations and emissions

In CMIP5, the models are driven by CO_2 concentrations in most of the runs and by CO_2 emissions in some of them (Taylor et al., 2011). These two classes of simulations can be performed with the full carbon-cycle configuration of the IPSL-CM5A-LR model (Fig. 1-c,d). For the interactive (i.e. fully coupled online) carbon cycle simulations, contrary to the cases of the chemistry and aerosols models, it is not the model itself which is expensive to run. The main difficulty lies in the estimation of the initial state of carbone stores , which requires very long runs to reach a steady-state. Even using some dedicated approaches to speed up the spin-up, a few hundreds of years of model integration are required in order for the various carbon pools to be close to equilibrium and hence can be used as initial states.

For the non-interactive (i.e. off-line) concentration-driven simulations from 1850 to 2300, CO_2 being well mixed in the atmosphere, the prescribed global CO_2 concentration is directly used by LMDZ to compute the radiative budget, and by the PISCES and ORCHIDEE models to compute air-sea CO_2 exchange and land photosynthesis respectively. The prescribed evolution of CO_2 concentrations is taken from the CMIP5 recommended dataset and are described in Meinshausen et al. (2011). For the historical period, (1850-2005), the CO_2 concentration has been derived from the Law Dome ice core record, the SIO Mauna Loa record and the NOAA global-mean record. From 2006 and onwards, CO_2 emissions have been projected by four different Integrated Assessment Models (IAMs) (van Vuuren et al., 2011), and corresponding CO_2 concentrations have been generated with the same reduced-complexity carbon cycle - climate model MAGICC6 (Meinshausen et al., 2011). In the RCP2.6 scenario, CO_2 concentration peaks at 440 ppmv in 2050 then declines. In the RCP6 and RCP4.5 scenarios, CO_2 concentration stabilizes at 752 and 543 ppmv in 2150 respectively. In the RCP8.5 scenario, CO_2 concentration reaches 935 ppmv in 2100 and continues to grow up to 1961 ppmv in 2250.

3.6 Other Green House Gas Concentrations

The greenhouse gases ozone are assumed to be well mixed in the atmosphere and are prescribed as time series of annual global mean mixing ratio. The concentrations of CH_4, N_2O, CFC-11 and CFC-12 are directly prescribed in the radiative code of LMDZ. The concentrations are taken from the recommended CMIP5 dataset[1] and are described in (Meinshausen et al., 2011). As the radiative schemes of GCMs do not generally represent separately all the

[1] see http://cmip-pcmdi.llnl.gov/cmip5/forcing.html

fluorinated gases that are emitted by human activities, the radiative effects of all fluorinated gases controlled under the Montreal and Kyoto protocols are represented in terms of concentrations of “equivalent CFC-12” and “equivalent HFC-134a”respectively. The “equivalent CFC-12” concentration is directly used in LMDZ whereas the “equivalent HFC-134a” is converted in “equivalent CFC-11” prior being used. For this conversion, we use the radiative efficiency of the two gases: $0.15\text{W.m}^{-2}.\text{ppb}^{-1}$ for HFC-134a and $0.25\text{W.m}^{-2}.\text{ppb}^{-1}$ for CFC-11 (Ramaswamy et al., 2001, Table 6.7).

3.7 Land use changes

To prescribed a common land use change in Earth System Models, and harmonization procedure has been proposed to produce a yearly global land-cover map, at 0.5°x0.5°, from 1500 to 2100,with a smooth transition between historical datasets and future projections (Hurtt et al., 2011). The historical datasets for croplands and pasture are from HYDE 3.1 (Klein Goldewijk et al., 2011). The maps of future projections of croplands and pasture are derived from each of the four Representative Concentration Pathways (RCP) produced by the corresponding Integrated Assessment Model (IAM) team. An anomaly verification procedure is done to ensure consistency between past and future changes. The overall croplands and pasture dataset is then combined to a specific land-cover map. This land-cover map is used for the information it provides on the relative proportion of the natural vegetation types, if any, at each grid cell. The resulting map is such that the extent, within one grid cell, of croplands and pasture is given by the reconstructed dataset mentioned above. The extent of the natural vegetation, within that same grid cell, is the complementary area. Therefore, this area might be wider or narrower than the one occupied in the land-cover map but the relative proportion of the natural vegetation types is preserved.

The land-cover map used to provide the relative proportion of the natural vegetation types is the ’home’ land-cover map, as described in Krinner et al. (2005), which is derived from Loveland et al. (2000). It shall be noted that in the case where the dynamics of the vegetation is activated, the ORCHIDEE model itself calculates the relative proportion of natural vegetation types.

3.8 Solar irradiance and volcanic aerosols

The IPSL model is directly forced by the annual mean of solar irradiance, again using the data recommended by CMIP (Lean, 2009; Lean et al., 2005). For the past periods, the estimate of the variations of the total solar irradiance (TSI) is the sum of two terms, the first is related to an estimate of the past solar cycles (Fröhlich and Lean, 2004) and the second to an estimate of the long term variations (Wang et al., 2005). For the future, it is assumed that there is no long term variations with repeated solar cycles that are identical to the last cycle (cycle 23), with solar irradiance values from 1996 to 2008 (Fig. 2, dot line). For other than historical and scenarios simulations, the TSI is held constant and equal to the mean TSI estimate between the years 1845 and 1855, i.e. 1365.7 Wm^{-2} (Fig. 2, dash line).

Volcanic radiative forcing is simply simulated by an additional change to the solar constant. For the historical period, the aerosol optical depth of volcanic aerosol is an updated version of Sato et al. (1993) obtained from http://data.giss.nasa.gov/modelforce/strataer/. The aerosol optical depth τ is converted to radiative forcing F_v (Wm^{-2}) according to the relationship $F_v = -23\ \tau$ proposed by Hansen et al. (2005). The average value $\bar{F_v}$ of this forcing over the period 1860-2000 is -0.25 Wm^{-2}, and the solar forcing F prescribed to the model is:

$$F = TSI + \frac{4(F_v - \bar{F_v})}{1-\alpha} \tag{1}$$

where $\alpha = 0.31$ is the planetary albedo. For the future scenarios, we assume that the volcanic forcing is constant, i.e. that a constant volcanic eruption produces a constant radiative forcing $F_v = \bar{F_v}$. This explains the jump of F between 2005 and 2006 (Fig. 2, continuous line); in 2005 there is almost no volcanic aerosols, as observed, whereas in 2006 a constant volcanic eruption that produces a constant radiative forcing starts.

[Fig. 2 about here.]

4 Recent and future global warming using SRES and RCP scenarios

The major advantage of the rather coarse resolution in the IPSL-CM5A-LR configuration, is that it is computationaly cheap. This permits us to cover in a reasonable amount of time, most of the long term simulations of CMIP5, that is the core, tier 1 and tier 2 long-term simulations. This efficiency is also useful to build up the initial states. In the following, we will describe how this initial state is prepared, as well as the key climatic variables simulated in the control, historical and scenario runs. We will also make some comparison with results obtained with the IPSL-CM4 model and that are in the CMIP3 data base. More comparison between the different versions of the IPSL model will be presented in section 6. More detailed aspects of the climate simulated by the IPSL-CM5A-LR model are in companion papers: like its global climatology in (Hourdin et al., this issue-a), its cloud properties in (Konsta et al., this issue), its tropical variability in (Maury et al., this issue; Kamala et al., this issue; Duvel et al., this issue), its mid-lattitude variability in (Vial, this issue; Cattiaux et al.), its climate over Europe in (Menut et al., this issue), and its simulation of the AMOC variability in (Escudier et al., this issue).

4.1 Initial state and control run

The initial state of the IPSL-CM5A-LR model has been obtained in four steps. First, a 2500 years long simulation of the oceanic model (without carbon cycle) has been done where the atmospheric conditions are imposed and correspond to the version 2 of the Coordinated Ocean-ice Reference Experiments (CORE) data sets (Large and Yeager, 2009). Second, the full carbon-cycle configuration of the IPSL-CM5A-LR model has been integrated for a period of 600 year, with the solar constant and the concentrations of the GHGs, and of the aerosols corresponding to their preindustrial values. Third, and because this last simulation is not long enough to bring the ocean and biosphere carbon pools at equilibrium, we have made stand alone few thousand of years long simulations with the ocean and land carbon cycle models (ORCHIDEE and PISCES). These offline simulations are forced by the atmospheric and oceanic variables from the preceding 600-yrs simulation and by a constant pre-industrial value for the atmospheric CO_2. Fourth, and after verification that the carbon pools are equilibrated, their values are included back into the complete IPSL-CM5A-LR model which is again integrated for another 400-yrs. At this time, carbon pools are close to equilibrium in the coupled model as well, and the control preindustrial simulations can start.

[Fig. 3 about here.]

To illustrate how well equilibrated our model is, the Fig. 3 shows the global average values of a few variables during the first 1000 years of the control: the surface temperature has almost no drift, the heat budget is close to zero, and there is no discernible difference between the flux at the TOA and at the surface. The surface salinity has almost no drift, as the sea surface height (about 2 cm/century, not shown), confirming that the water cycle is well closed. Also, there is no drift of the carbon flux over land and there is a small drift of the carbon flux over oceans, which begins from 0.4PgC/yr and slowly decreases to reach less than 0.1PgC/yr at the end of the 1000 years period.

4.2 Recent warming and current mean temperature

The Fig. 4-a displays the time evolution of the global mean air surface temperature from observations (in red, Hadcrut3v dataset, Jones et al., 1999; Brohan et al., 2006), simulated by the IPSL-CM5A-LR (black line) for CMIP5, and by IPSL-CM4 (green line) for CMIP3. For completeness here, we also show the results from IPSL-CM5A-MR. As expected, all the historical simulations indicate a substantial global warming induced by increased concentrations of greenhouse gases in the atmosphere. For both models, the global trend and pluri-annual variabilities agree rather well with observations, but the simulations of the twentieth-century climate change realized with IPSL-CM5A (LR and MR) are significantly better than the simulations done with IPSL-CM4. This was expected as the IPSL-CM5A models include more realistic ozone, aerosols, and solar forcings (including volcanoes) than IPSL-CM4.

[Fig. 4 about here.]

To extract more precisely the temperature trends, the time series of the monthly temperature from the simulations and the observations (HadCRUT3v) were subjected to the STL (Seasonal-Trend decomposition procedure based on Loess) additive scheme, a powerful statistical technique for describing a time series (Cleveland et al., 1990). In the STL procedure, the analyzed X(t) monthly time series is decomposed into three terms:

$$X(t) = T(t) + A(t) + R(t) \qquad (2)$$

The T(t) term is used to quantify the trend and low-frequency variations in the time series. The A(t) term describes the annual cycle and its modulation through time. Finally, the R(t) term contains the interannual signal and the noise present in the data. All the terms are estimated through a sequence of applications of locally-weighted regression (or loess) to data windows whose length is chosen by the user. The STL procedure is an iterative process, which may be interpreted as a frequency filter directly applicable to non-stationary data (Cleveland et al., 1990). Other important features of

STL is the specification of the amounts of seasonal and trend smoothing, the ability to produce robust estimates of the trend and seasonal components that are not distorted by aberrant or extreme behaviors in the data and the stationarity of the R(t) time series. As demonstrated by Morissey (1990) or Terray (2011), this procedure is particularly useful for extracting the interannual and trend signals from non-stationary and noisy climate datasets. Thus, the STL procedure is particularly well adapted here to estimate and objectively compare the trends in observations and historical simulations. Finally, note that, in order to be consistent with monthly temperature observations available from the HadCrut3v dataset (Brohan et al., 2006), all the simulated grid-box temperature time series are first expressed as monthly anomalies from the 1961-1990 climatology simulated by each model's configuration before computing the global area-averaged time series and running the STL statistical procedure. This pre-processing of all the time series, which is justified for the observations in order to avoid biases that could result from the elevation of stations on land or from the various methods used to compute monthly temperature in different countries (see http://www.cru.uea.ac.uk/cru/data/temperature/ for further details) is normally not required for the simulations, but will allow here a fair comparison of the temperature trends in observations and the various simulations.

Figure 4-b presents the trends as estimated by the STL decomposition illustrating that important features appear much more clearly when using this procedure. The first is that the IPSL-CM4 simulation does not reproduce the two coolings that are observed around 1910 and 1960 respectively. Conversely the IPSL-CM5A-LR model does simulate the cooling around 1960, whereas the 1910's cooling is predicted to soon by the model. These relative successes in producing the coolings in the new version essentially comes from the inclusion of the volcanoes. Also, IPSL-CM5A simulates a larger temperature increase than IPSL-CM4 after 1970. During this period, the difference is probably due to the changes in ozone concentrations and absorbing aerosols concentration, both of them increasing significantly after 1950. However, for IPSL-CM5A-LR, the different run members exhibit a very different trend between 1970 and 2005, which make it difficult precisely quantified this effect. Compared with observations, IPSL-CM5A-LR.seems to overestimate the warming tendency during recent decades, even one may not exclude that this difference is partly due to internal variability.

Despite the fact that the model warming is too fast during the late 20th century, it should be emphasized that the model is nevertheless quite cold. More specifically, the surface temperature simulated by IPSL-CM5A-LR over the 1961-1990 period has an 1.3^oC cold bias. This cold bias is more pronounced in the mid latitudes (Fig. 5), even if the zonal distribution of temperature is better simulated in IPSL-CM5A-LR than in the previous version, IPSL-CM4 (Marti et al., 2010). The geographical distribution of the temperature bias does not change much along the seasons (Fig. 5-b). The most important change are at high latitudes: the warm bias over Siberia and Alaska increases and extends over Europe and North America during boreal spring and summer and the warm bias over the southern ocean is maximum in austral summer.

[Fig. 5 about here.]

4.3 Future warming projections using RCP scenarios

In the various scenarios in Fig. (Fig. 6-a) the temperature increase is quite similar during the first three decades (2005-2035), whereas during the same period, the net heat flux at the TOA start to differ (Fig. 6-b). These differences become more pronounced thereafter, and start to affect the evolutions of the temperature. At the end of the 23rd century, the difference in temperature becomes as large as 11°C between the highest (RCP 8.5) and the lowest (RCP 2.6) scenarios. For the low RCP 2.6 scenario, the radiative forcing decreases and the temperature is almost constant from 2050 onward. It even slightly decreases despite a positive net flux at the TOA thanks to a heat uptake by the ocean (not shown).

[Fig. 6 about here.]

A multitude of factors affect the local temperature changes. A first factor is the geographical distribution of the forcings, like the aerosols concentration or the land use. A second factor is the geographical distribution of the climate response to these forcings, and in particular the strength of the local feedbacks. In order to separate the geographical distribution pattern from the global mean value, we define the local temperature amplification factor as the ratio between the local temperature change and the global mean temperature change. The zonal mean average of this temperature amplification has been shown to be little dependent on the scenario for the CMIP3 simulations (Meehl et al., 2007b). As in CMIP5, more forcings with a strong local signature are considered (land use, black carbon...), a different answer could be expected. As shows Fig. 7 for the two extremes RCP scenarios (RCP 2.6 and RCP 8.5), this is not quite the case. The general pattern of temperature change is the one that is classically obtained. More specifically, there is a larger temperature increase over continent than over ocean, a strong amplification in the arctic regions, whereas the smallest warmings are found over the southern ocean. At the end of the 21st century (upper row), the geographical pattern of the local temperature amplification is very similar in both RCP 2.6 and RCP 8.5 scenarios, as they are for the two others (RCP 4.5 and RCP 6.0, not shown). However, the continental warming is generally more extended for RCP8.5.

[Fig. 7 about here.]

At the end of the 23rd century, the differences among geographical patterns of temperature amplification in the two extremes scenarios are larger, even though they remain surprisingly small compared to the very large differences between the two global mean temperature changes: 1.9K for RCP 2.6 and 12.7K for RCP8.5. Continental warming is again more extended in the stronger scenario. The relatively small polar warming in RCP8.5 reflects a very different polar amplification which will be analyzed below (section 5.3). For the RCP2.6 scenario, there are little differences between the end of the 21st and 23rd century. In particular, the small warming simulated in the southern ocean at the end of the 21st century is still present 200 years later. For the RCP4.5 scenario, the pattern of the local temperature amplification in 2300 is very closed to that of scenario RCP2.6 (not shown). In the case of RCP8.5, the warming is more homogeneous as simulated at the end of the 23rd century than during the 21st century.

4.4 Future warming projections using SRES scenarios

In this section, we will compare the temperature increases and the radiative forcings of the SRES scenarios that were used in CMIP3 with those of the RCP scenarios that are used in CMIP5. With the same model, IPSL-CM5A-LR, we will perform simulations with both the SRES and RCP forcings. For the greenhouse gas, the concentration of the different long-lived greenhouse gases are fully specified in both SRES and RCP, which is not the case for ozone. Here we assume that the ozone concentration of the SRES-A2, SRES-A1B and SRES-B1 scenarios are the same as the ozone concentration of the RCP 8.5, RCP6.0 and RCP4.5 scenarios, respectively. For the aerosols, little information was given for the SRES scenarios whereas this information is available for the RCPs. Therefore, we consider six types of aerosols in RCP simulations (see section 2.2.3) but only the sulfate aerosol in SRES runs. For the SRES scenarios we take the sulfate aerosol concentrations computed by Pham et al. (2005) and, to avoid a discontinuity of forcings at the beginning of these scenarios, we first made an historical simulation using the consistent distribution of sulfate aerosols (Boucher and Pham, 2002). For the land use changes, again they are considered in the RCP runs but not in the SRES runs, for which the land use of year 2000 is kept for the whole 21st century. These choices are consistent with the fact that in CMIP3 most models consider forcing by ozone and sulfate aerosol but neither the forcing due to other aerosols species nor the forcing due to land use changes, whereas for CMIP5, most models are expected to consider a larger variety of aerosol as well as the land use changes.

Compared to the SRES scenarios, the spread of future global warming for the RCP scenarios is much larger (Fig. 8). The RCP8.5 scenario leads to a higher warming than the SRES-A2 scenario, and RCP2.6 leads to a stabilization of the global mean surface temperature from 2040, a features that none of the SRES scenarios simulates. Also, the corresponding RCP and SRES projections often differ significantly except maybe the RCP 4.5 and SRES-B1 simulations. For these two scenarios, the long-lived greenhouse gases (LLGHG) forcing and the temperature increase are very close, although the simulated temperature increase is a bit smaller around 2040 for SRES-B1 compared to RCP 4.5 due to the radiative effect of aerosol that is larger for SRES-B1.

The aerosol radiative forcings is very difference between the two families of scenarios. One difference is that aerosol concentrations is maximum around 2020 and then decreases in the RCP family, whereas the aerosol concentrations increases until 2030-2050 in the SRES family. The second difference is that we consider only the sulfate aerosol in the SRES experiments whereas absorbing aerosols are also considered in the RCP experiments, which strongly reduces the total aerosol radiative forcing. However, for all the scenarios, the contribution of the anthropogenic aerosols forcing relative to the total anthropogenic forcing is smaller in 2100 than in 2000.

A common feature that can be observed in the results of both families of scenario is the delay between the difference in radiative forcing and in temperature increase. The difference in radiative forcing between SRES-A2 and A1B scenarios on one side, between RCP6.0 and RCP4.5 on the other side, started around 2060. The change in temperature increase is apparent twenty years later, but is still not very high at the end of the century.

[Fig. 8 about here.]

4.5 Computing the CO_2 flux and the compatible emissions of CO_2

For the historical period, and for each of these scenarios, the land (ORCHIDEE) and ocean (PISCES) carbon cycle models generate spatially-explicit carbon fluxes in response to atmospheric CO_2 concentration and simulated climate. The simulated net land carbon flux does include a land-use component, but we have not yet analyzed this net flux into its land-use and natural parts. Piao et al. (2009) however did show that a similar version of ORCHIDEE was able to reproduce estimated land use change related carbon emissions when forced over the historical period by the Climate Research Unit temperatures and precipitations.

In the historical simulations, the net ocean and land fluxes increase to reach 2.2 (± 0.05) and 1.28 (± 0.1) Pg/yr in the 1990-1999 decade respectively (Fig. 9). These values are in the range of the recent estimations of Le Quéré et al. (2009) for the 1990-1999 decade: 2.2 ± 0.4 PgC/yr for the ocean and 1.1 ± 0.9 PgC/yr for the land.

Over 2005-2300, the ocean uptake increases up to 6 PgC/yr in 2100 for the RCP8.5 scenario. For the RCP6.0 and RCP4.5 scenarios, the ocean uptake peaks at 5 PgC/yr in 2080, and at 3.7 PgC/yr in 2030 respectively, before decreasing towards the end of the simulation. For the RCP2.6 scenario, the ocean uptake does not exceed 3.2 PgC/yr and almost tends towards zero in 2300. Over 2005-2300, the differences in net land flux between the different scenarios is much less clear. The net land flux (including land-use emissions) peaks at 5 PgC/yr in the RCP8.5, RCP6.0 and RCP4.5 during the course of the 21st century. For the RCP2.6 scenario, the net land flux does not exceed 3 PgC/yr. After 2150, the net land flux is close to zero or negative for all tested scenarios (i.e. the land is a source of carbon to the atmosphere).

We also diagnosed compatible emissions from the simulated land (F_l) and ocean (F_o) carbon fluxes and prescribed CO_2 concentrations using the following equations for emission rates

$$F_e = \frac{M_C}{dt} + (F_o + F_l) \tag{3}$$

where M_C is the mass of carbon in the atmosphere. As ORCHIDEE explicitly simulates the natural and the land-use component of land-atmosphere carbon fluxes, our compatible emissions refer here to fossil-fuel + cement production only emissions. We display Fig. 10 the computed compatible emissions for the historical and RCPs simulations.

For the 1990-1999 decade, our compatible emissions amount to 6.6 (± 0.2) PgC/yr, which compares well with data-based estimates of 6.4 (± 0.4) PgC/yr (Forster et al., 2007). In 2100, the cumulative compatible emissions largely differ between the scenarios and amount to 2288 (±3), 1644, 1349 (± 10), 793 (±1) PgC, for the RCP8.5, RCP6.0, RCP4.5 and RCP2.6 respectively. Our cumulative emissions also differ from the initial IAMs (Integrated Assesment Models) emissions. For the RCP8.5 scenario, the IAM emissions amount to 2521 PgC in 2100 whereas we obtain a significantly lower number with 2288 PgC. For the RCP2.6 scenario however, the IAM emissions and our estimates agree (790 PgC each). In 2300, our cumulative compatible emissions are 4946, 1797 and 627 PgC for the RCP8.5, RCP4.5 and RCP2.6 respectively. Interestingly, the RCP2.6 compatible emissions reach negative values from 2100 onwards.

[Fig. 9 about here.]

[Fig. 10 about here.]

5 Futur climate changes with RCP scenarios

In this section, we analyze some aspects of climate change as simulated by the IPSL-CM5A-LR model for the RCP scenarios.

5.1 Futur precipitation changes

Fig. 11 presents the 10-year annual mean of rainfall for IPSL-CM5A-LR averaged over the last decade of the 20th century, together with GPCP (Global Precipitation Climatology Dataset) observations (Huffman et al., 2001) averaged over the same period. The IPSL-CM5A-LR model is able to reproduce the main structures of the observed precipitation pattern. In the tropics, though, the model shows a so-called double ITCZ structure, with a first, realistic, precipitation maximum around 5^{o}N and a secondary convergence zone around 5^{o}S. Also the monsoon rainfall over West Africa and Indian sub-continent does not sufficiently extend to the north. In the southern subtropics, the model fails to simulate the large regions without any rain that are observed over ocean. Over Africa and the Arabian peninsula, this area is on the contrary too extended.

[Fig. 11 about here.]

The global mean precipitation change in a warming climate is now well understood as it is primary the result of changes in the energy balance of the atmosphere (e.g. Allen and Ingram, 2002; Held and Soden, 2006; Takahashi, 2009). Indeed, the latent heating coming from precipitation is the main heat source that compensate the radiative cooling of the atmosphere, the sensible heat playing only a secondary role. The precipitation changes are therefore mainly driven by the changes of the radiative budget of the atmosphere and are about 2% K^{-1} in response to a CO_2 forcing according to theoritecal and multi-model studies by e.g. (Allen and Ingram, 2002; Held and Soden, 2006). In IPSL-CM5A-LR, it amounts 2.2%K^{-1} for the RCP 8.5 scenario (not shown), which is largely consistent with these previous studies.

To look at the geographical distribution of the precipitations and to allow a better comparison between the different scenarios, we will use the "normalized relative precipitation change", i.e. the relative change of precipitation (dP/P computed at each grid point) normalized by the global temperature change. Units are thus % K^{-1}. The geographical distribution of the normalized relative precipitation changes at the end of the 21st century shows well known general patterns, with a relative decrease of precipitation in most of the subtropics and an increase mainly in the equatorial regions and at mid and high latitudes (Fig. 12). In other words, rainy areas tend to become wetter and conversely. However, the similarity of the patterns of precipitation changes for the different RCPs scenarios, despite the differences in the forcings, is puzzling. The regions where the precipitations decrease are almost the same for all the scenarios, both over ocean and land, and the normalized amplitudes are very comparable. Over north Asia and north America, the regions where precipitations increase are very similar, but the normalized amplitude is a bit larger for the lower scenarios (RCP 2.6) than the higher scenario (RCP 8.5). This is consistent the results by Johns et al. (2011).

[Fig. 12 about here.]

5.2 Atlantic meridional overturning circulation

The Atlantic Meridional Overturning Circulation (AMOC) maximum is represented Fig. 13 for different simulations of the IPSL-CM5A-LR model. This index represents the strength of circulation meridional streamfunction over the North Atlantic (30-80°N, 500-5000m) and the amount of ocean water sinking at depth in the North Atlantic. In the control simulation, the AMOC is too weak in this model, due to a lack of convection in the Labrador Sea as in previous versions of the IPSL model (Swingedouw et al., 2007a; Marti et al., 2010). This bias has not been resolved and is mainly related to a shift of the atmospheric zonal wind stress towards the equator. Over the historical era, the AMOC maximum is very similar to that from the control simulations. We notice a slight increase in the 70's and then a plateau of relatively high AMOC intensity as compared to the control simulation. This behavior is discussed in (Swingedouw et al., this issue). In all the projections, the AMOC weakens from 2020 onward and its intensity is weaker than in the control run by 2050. On the longer time scale, the projections that have been extended (RCP26, RCP45 and RCP85) show very different behaviors. RCP26 show a clear recovery from 2100 and reaches the control value around 2200. RCP45 presents a slight recovery, rather a stabilization around 8 Sv from 2150, while RCP85 exhibits a continuous decrease down to less than 4 Sv in 2300. Such a state can be considered as a collapse of the AMOC (not shown).

To further explain the responses of the AMOC, we analyze the evolution of deep convection in the northern North Atlantic. These areas have been identified in (Escudier et al., this issue)for this model, and are shown to drive the AMOC variability. Figure 14-a shows in particular that the low frequency changes of mixed layer depth (MLD) averaged over these areas lead variations in the AMOC by around a decade: a slight increase in the 60's in the historical simulations, leading the AMOC increase in the AMOC, and a weakening of deep convection in the projections from around 2010, followed by different behaviors in the longer term depending on the scenario (recovery in RCP26 and RCP45 and collapse in RCP85). The MLD is well correlated (in phase) with the surface density in the convection sites (Escudier et al., this issue), which is indeed the trigger for deep convection. The surface density can be decomposed into haline and thermal components after linearization. This allows identifying whether the changes in the MLD are due to a change in salinity or temperature. Fig. 14.c and d show that the thermal component is decreasing in all the simulations as soon as the 60's. On the other hand, the haline component has a more complex behavior. It increases in the 60's and remains higher than the control simulations in all the projections up to 2060 at least. Later, it decreases steeply in the RCP85 long projections while it remains at the control simulations level in RCP45 and even above in RCP26.

Our interpretation of this behavior is the following. The increase in local SST is part of the increase of the global surface temperature in response to the increase of GHG. The increase in sea surface salinity from the 60's is the result of the balance between two opposed effects: the transport of saltier waters from the tropics where the evaporation increases (not shown) and precipitation decreases on the one side, the increase in precipitation and runoff in the high latitude on the other side. It seems that in this model the balance is at the advantage of a salinification of the North Atlantic, which stabilizes the AMOC, as it was the case in the former version of this model (Swingedouw et al., 2007b). The total evaporation integrated over the whole Atlantic (from 30°S and including the Arctic basin) rises from 0.49 Sv in control simulations (the Atlantic basin is an evaporative one as in the real system) up to 0.62, 0.65 and 1.23 Sv for the last 30 years of RCP26, RCP45 and RCP85 respectively. This is associated with a large increase in the fresh water export by the atmosphere from the Atlantic to the Pacific, as it was the case in IPSL-CM4 (Fig. 11 from Swingedouw et al. (2007b)). Nevertheless, because of the thermal component that tends to weaken deep convection in the northern North Atlantic, the AMOC gradually weaken. For a sufficient weakening (as in RCP85), of this large scale northward transport of heat and salt towards the North, an oceanic feedback becomes dominant: the northward oceanic salinity transport associated with the AMOC decreases, leading to a decrease in sea surface salinity in the convection sites and a collapse of the AMOC. This mechanism is the so-called Stommel positive feedback, (Stommel, 1961). It explains the negative contribution of the haline component of density in RCP85 from around 2060 (Fig. 14.c).

It should be noticed that in the IPSL-CM5A-LR model, the melting from Greenland ice sheet is not taken into account, although it can have a large impact on the AMOC (Swingedouw et al., 2007b). The analysis of such an effect will be realized through the coupling of IPSL-CM5A-LR with a Greenland ice sheet model, which will be presented in a future study.

[Fig. 13 about here.]

[Fig. 14 about here.]

5.3 Polar amplification and sea-ice extent

Due to the large extent of snow and ice covered surfaces over polar areas and their significant decrease with global warming, specific feedback mechanisms take place at high latitudes (Manabe and Stouffer, 1980). Indeed snow and ice are strongly sensitive to air temperature, but they also strongly affect the surface energy budget by increasing the surface albedo and thermally isolating the oceanic surface from the air. As a result, the temperature increase with global warming in the Arctic simulated by most models is large (Meehl et al., 2007b), and it is alson the case for the IPSL-CM5A-LR model (Fig. 7).

To quantify this effect, the polar amplification is defined here as the ratio between the mean increase of surface air temperature poleward of the Arctic or Antarctic circle respectively, and the globally averaged temperature increase. To better understand the relationships between polar amplification and sea ice extent, we also compute the total sea ice extent in September for each scenario. The reason is that September is the month during which this extent is minimum, and thus it is the month during which the Arctic Ocean is predicted to first become seasonally free of ice (Fig. 16). In the Southern Ocean, summer sea ice area is limited by the presence of the Antarctic continent, situated over the pole. Therefore, Antarctic sea-ice extent is more sensitive to climate change in winter than in summer.

[Fig. 15 about here.]

Figure 15 shows the thermal polar amplification for the Arctic (top) and Antarctic (bottom) until 2300. The amplitude of the natural variability is large for all the scenarios, in particular during the initial 25 years (dashed lines). By the end of the 21st century (date for which simulations for all scenarios are available) the warming in the Arctic as projected by IPSL-CM5A-LR will roughly reach twice the global value whatever the scenario is. In the RCP8.5 scenario, the Arctic ocean will be free of ice at the end of summer by 2070 (Fig. 16), and about 30 years after, after some weak oscillations, Arctic amplification will slowly and continuously decrease. In the RCP4.5 scenario, the Arctic is never projected to become free of sea ice, but the sea ice extent decreases to about a fifth of its present day value. The Arctic amplification in RCP 2.6 displays the highest variability, in agreement with pronounced sea ice extent variability, and no clear trend either. This strong variability in RCP2.6 might come from a seasonal effect. Indeed if summer Arctic amplification strongly depends on sea ice cover, snow covered areas are the main source of winter Arctic amplification variability (Hall, 2004). Given that snow extent is larger, and potentially more variable, in the lowest scenario (RCP2.6), the impact of land covered with snow might be one cause of the high arctic amplification variability in RCP2.6. Another reason is, more generally, that the global and regional mean climate change signal in RCP2.6 is or course weaker than in the other scenarios. Therefore the computed polar amplification is necessarily more strongly affected by internal variability on all relevant spatial and temporal scales.

In the Southern hemisphere, the polar amplification we compute is very clod to one. Austral amplification mostly takes place over sea ice, and decreases poleward (Hall, 2004), and is therefore not included in the area for which we chose to compute the polar amplification (Fig. 7). Again, variability is highest in the lowest RCP scenario, and strongly correlated with sea ice extent. Unlike in the Northern hemisphere, seasonal snow cover in the Southern hemisphere is small. Therefore, via the snow-albedo feedback mainly in summer and its effect on ocean-atmosphere heat fluxes mainly in winter, sea ice is the most obvious polar surface amplifier of mean climate change and internal variability, and the two sets of curves are indeed highly correlated. The warming over the Antarctic continent will only reach the global value in the RCP 8.5 scenario around 2300. Large effective heat capacity of the Southern Ocean delays the Antarctic warming.

[Fig. 16 about here.]

6 Influence of changes in models on climate variability and climate sensitivity

The IPSL-CM4 model has been used for CMIP3, and for CMIP5 three different versions of the IPSL-CM5 model are currently used: IPSL-CM5A-LR for which most of the results have been shown so far, IPSL-CM5A-MR which is the same model with a higher horizontal resolution of the atmosphere (1.25°x2.5°, see section 3.2) and IPSL-CM5B-LR for which the atmospheric parameterizations have been strongly modified (see section 2.2.1). The key climatic characteristics of IPSL-CM4 have been presented in Marti et al. (2010) and Braconnot et al. (2007). A comparison of some basic characteristics of IPSL-CM4, IPSL-CM5A-LR and IPSL-CM5A-MR climatology is presented in (Hourdin et al., this issue-a), and some key differences between IPSL-CM5A-LR and IPSL-CM5B-LR are presented in (Hourdin et al., this issue-b). Here we will first focus on how these different models simulate two major modes of tropical variability, ENSO and the MJO. These modes have a large impact on the tropical and global circulation (e.g. Cassou, 2008; Alexander et al., 2002; Maury et al., this issue) and there is a large diversity of their representation in climate models (e.g. Guilyardi et al., 2009; Xavier et al., 2010). Then we will compare their climate sensitivity, i.e. their surface temperature response to an increase of the concentration of CO_2 as the patterns of the air surface temperature response and the precipitation response.

6.1 Impact on Madden-Julian Oscillation

The impact of the new physics on the simulated MJO is stronger during boreal winter. We thus restrain here our presentation to the January-March period (JFM). A more complete study of the intraseasonal variability and the MJO can be found in a companion paper (Duvel et al., this issue). The large-scale convective perturbations associated with the MJO are extracted with the Local Mode Analysis (LMA, Goulet and Duvel, 2000). The LMA is based on a series of complex EOF (CEOF) computed on relatively small time sections (every 5 days on a 120-day time window) of the outgoing longwave radiation (OLR) time series. The first complex eigenvector best characterizes (phase and amplitude) the intraseasonal fluctuation for the 120-day time section. The corresponding percentage of variance represents the degree of spatial organization of this event. The LMA retains only maxima in the percentage of variance time series. For JFM, the LMA extracts 41 events for 30 years of observations (NOAA OLR, Liebmann and Smith, 1996), 52 events for 30 years of CM5A-LR and 34 for 25 years of CM5B-LR. The average period for these events is roughly 40 days for all three datasets.

[Fig. 17 about here.]

An average pattern is also computed from the JFM events having a percentage of variance above the annual average. This average pattern gives amplitude and phase distributions that best represent the events considered. Figure 17 shows maps of JFM average amplitude for observations, CM5A-LR and CM5B-LR together with the average pattern. In observations, the intraseasonal variability is confined between the equator and 20°S. The average pattern reflects the expected eastward propagation of about $5ms^{-1}$ (Fig. 17-a). IPSL-CM5A-LR produces MJO events confined in the Indian Ocean and that propagates eastward at around $2ms^{-1}$ only (Fig. 17-b). IPSL-CM5B-LR produces perturbations more centered on the Maritime Continent and propagating at a speed of about $2.5ms^{-1}$ (Fig. 17-c). The longitudinal position of the main MJO signal is thus improved in CM5B-LR for the JFM season. However, the slow propagation and the too strong variability north of the equator remain. The ability of a model to organize convective perturbations at large scale is critical for a correct simulation of the intraseasonal variability (Bellenger et al., 2009; Xavier et al., 2010). This organization is indeed necessary to trigger the basin-scale dynamical response to the convective heating that drives the evolution of the perturbation at the planetary-scale. The contour on figure 17 measures the degree of large-scale organization of the intraseasonal variability. Within this contour, the intraseasonal variability is mostly due to the large-scale organized perturbation (the first CEOF) obtained by the LMA. In the observations the intraseasonal variability of convection is mainly due to organized convection. However, CM5A-LR and CM5B-LR are unable to produce such organized convection (Fig. 17-b-c).

6.2 Impact on El Niño Southern Oscillation

The ENSO spatial structure of the 3 models, as measured by the SST standard deviation, is compared to observations in Fig. 18. We used 200 years of CM4 and CM5A-LR monthly outputs, whereas only 100 years from CM5B-LR are available. The new versions produce a weaker ENSO SST variability (by about 0.3K) with a pattern in qualitative good agreement with the observations. Interestingly, the spurious westward extension of the SST pattern is reduced in CM5B-LR when compared to CM4 and CM5A-LR. It has to be noted that the three versions show in addition a relative underestimation in the SST variability along the South America coast that is related to a common warm bias in the region.

ENSO spectral characteristics may be delicate to be estimated from 200 years or shorter time series (Wittenberg, 2009). However, Niño3 SST monthly anomalies spectra are indicative of an ENSO with longer periods in the later versions of IPSL-CM. Spectral peaks around 3-3.5 years are visible for CM5A-LR and B whereas CM4 shows a peak around 2.7 years (Fig. 19-a). CM5A-LR shows a good qualitative agreement with the observations showing a second spectral peak above 4 years. ENSO is in addition characterized by a strong seasonal phase locking with a peak in November-January and a minimum in April. This seasonality is well reproduced by CM4 but the new versions fail at reproducing this feature (Kamala et al., this issue). CM5A-LR shows a marked seasonality with a peak in May-June and a minimum in October-November, whereas CM5B-LR hardly shows any seasonal variation.

[Fig. 18 about here.]

[Fig. 19 about here.]

A number of studies point to a dominant role of the atmospheric GCMs in the simulation of ENSO in models (Guilyardi et al., 2009; Kim and Jin, 2011; Clement et al., 2011). The main atmospheric feedbacks are evaluated following (Lloyd et al., 2011a,b). The Bjerkness feedback is evaluated by the linear regression coefficient between the zonal wind stress anomaly in Niño4 and the Niño3 SST anomaly. The heat flux feedback is evaluated by the regression coefficient between Niño3 heat flux and SST anomalies. This feedback is dominated by the shortwave and the latent heat fluxes and the former has a key role in explaining the diversity of ENSO characteristics among models (Lloyd et al., 2011b). Fig. 19-b presents the process-based metrics associated to these atmospheric feedbacks. CM5B-LR shows a better agreement with the reanalysis than CM4 and CM5A-LR for all the four process-based metrics. Both Bjerkness and heat flux feedbacks are stronger in CM5B-LR and closer to the observations. In particular, the stronger heat flux feedback is due to a better simulated latent feedback and an improvement in the shortwave feedback that has the right sign compared to CM4 and CM5A-LR. This change in the shortwave feedback sign is probably linked with the type of clouds that the model produces in the Niño3 region. In summary, the IPSL-CM5 (A and B) tends to have a weaker and more realistic ENSO than CM4, it is moreover linked with a better representation of atmosphere feedbacks in CM5B-LR.

6.3 Impact on Climate sensitivity and feedbacks

To estimate the temperature response to an increase of the CO_2 concentration, two types of experiment are particularly useful in CMIP5: the so-called 1%-per-year experiment in which, starting from the control run, nothing is changed except the CO_2 concentration which increases by 1%-per-year until a quadrupling of its initial value (i.e. after 140 years) and the so-called abrupt $4CO_2$ experiment in which the CO_2 concentration is instantaneously increased to 4 times its initial value and is then held constant. This later experiment does not exist for the IPSL-CM4 model as it does not belong to the CMIP3 experimental design.

In order to analyse these experiments we shall use the feedback analysis framework with the same notation as in Dufresne and Bony (2008), where more details can be found. In response to a radiative forcing at the TOA ΔQ_t, the changes of the surface temperature ΔT_s and the radiative flux at the TOA ΔF_t are approximately related through the following equation:

$$\Delta T_s = \frac{\Delta F_t - \Delta Q_t}{\lambda}. \quad (4)$$

where λ is called the "climate feedback parameter" (fluxes are positive downward). Within this framework, when the model reaches a new equilibrium after a constant forcing has been applied, the net flux at the TOA ΔF_t tend toward zero, yielding an equilibrium temperature change $\Delta T_s^e = -\Delta Q_t/\lambda$.

The definition of the forcing ΔQ_t is not unequivocal. In the most usual definition until now, this forcing is computed assuming an adjustment of the temperature of the stratosphere (e.g. Forster et al., 2007). Using off-line calculation with stratospheric adjustment, we obtain $\Delta Q_t(2CO_2) \approx 3.5 W.m^{-2}$ ($3.7 Wm^{-2}$ in clear sky conditions) for a doubling of the CO_2 concentration, and the double of this value ($\Delta Q_t(4CO_2) \approx 7.0 W.m^{-2}$, ($7.4 Wm^{-2}$ clear sky)) for a quadrupling of the CO_2 concentration. We obtain the same values for the IPSL-CM4 and IPSL-CM5A model. For intermediate values x of the ratio between the CO_2 concentration and its preindustrial value, the radiative forcing is estimated using the usual relationship: $\Delta Q_t(x) = \Delta Q_t(2CO_2).\log(x)/\log(2)$. Using this forcing and the results of the 1%-per-year experiment, we compute time series of the climate feedback parameter λ for the different version of the IPSL-CM model, except for IPSL-CM5B-LR for which the results are not yet available. The values reported in Table 1 are the 30 year average value of λ around the time of CO_2 doubling (i.e. between year 56 and 85). The feedback parameter λ for IPSL-CM5A-LR is very close to that of the previous version, IPSL-CM4. It is also almost equal to that of IPSL-CM5A-MR that only differs by the horizontal resolution of the atmospheric model. The same results apply for the equilibrium temperature change $\Delta T_s^e(2CO_2)$ for a doubling of the CO_2 concentration (often called "climate sensitivity").

[Table 1 about here.]

Another classical metric to characterize the response to an increase of the CO_2 concentration is the "transient climate response" (TCR), i.e. the air surface temperature increase in a 1%-per-year experiment when the CO_2 concentration has doubled, i.e. 70 years after it has started to increase (here we computed the 30 year average, i.e. the average between year 56 and 85). We obtain (Table 1) that this transient temperature change is exactly the same for IPSL-CM5A-LR and IPSL-CM5A-MR that only differs by the horizontal resolution of the atmospheric model, a result obtained by Hourdin et al. (this issue-a) with a broader range of horizontal resolution of the atmospheric model. But this transient temperature change is lower for the IPSL-CM4 model than for IPSL-CM5A-LR , although its equilibrium temperature change $\Delta T_s^e(2CO_2)$ is a little higher. This probably means that the difference in transient temperature change originate from the ocean model, which effect on surface temperature is zero at equilibrium but not in transient conditions, within this framework.

As stated before, the definition of the forcing ΔQ_t is not unequivocal and recent work shows that the decomposition of the forcing in a fast and a slow part allows to better analyze and better understand the temperature and precipitation responses to a CO_2 forcing (Andrews and Forster, 2008; Gregory and Webb, 2008). The forcing including the fast response can be obtained using the abrupt 4xCO2 experiment (Gregory et al., 2004). Indeed, in response to a constant forcing, Eq. 4 simplified: The slope of the regression of the net flux at TOA as a function of the global mean surface temperature provide an estimate of climate feedback. The intercept of the regression line and the Y axis ($\Delta T_s = 0$) is an estimate of the radiative forcing including the fast response of the atmosphere. The intercept of the regression line and the X axis ($\Delta F_t = 0$) is an estimate of temperature change at equilibrium ΔT_s^e. Here we suppose that the radiative forcing and the temperature change at equilibrium for a doubling of CO_2 are half of the values for a quadrupling of CO_2. For the IPSL-CM5A-LR model, the radiative forcing obtained with this method is only slightly smaller than the classical one: 3.3 instead of 3.5 Wm^{-2} (Table 1). However, this result masks the large variation of the forcing in the shortwave and longwave domain that compensate each other. With this method, the feedback parameter is significantly smaller (in absolute value) and the temperature change at equilibrium is significantly larger than the one obtained with the 1%-per-year experiment. This difference in temperature change at equilibrium should be zero if the two methods and the feedback framework were perfect, which is not the case. It is therefore important to compare values that have been estimated with a very same method.

An important result for the IPSL-CM5 is the very strong difference between the climate sensitivities obtained with IPSL-CM5A-LR and IPSL-CM5B-LR. While the climate sensitivity simulated by IPSL-CM5A-LR ($\Delta T_s^e(2CO_2) \approx 3.9K$) lies in the upper part of the sensitivity range of the model that contribute to CMIP3, IPSL-CM5B-LR sensitivity ($\Delta T_s^e(2CO_2) \approx 2.4K$) falls in the lower part (Meehl et al., 2007b). The analysis of the reasons of these differences require further work that will be presented in a forthcoming paper.

6.4 Patterns of changes in surface air temperature and in precipitation

As illustrated in previous sections, the normalized patterns of temperature and precipitation changes are very little dependent on the scenario (Fig. 7 and 12). Here we will illustrate if and how they are sensitive to the version of the IPSL-CM model that is used.

We will use the results of the 1%-per-year experiment for all models but IPSL-CM5B-LR for which we will use the abrupt 4CO2 experiment. For the 1%-per-year experiment, the temperature and precipitation changes are computed over a 30 year average period around the time of CO_2 doubling, i.e. between year 56 and 85 after the beginning of the experiment, as in section 6.3. For the abrupt 4CO2 experiment with the IPSL-CM5B-LR model, we compute the average temperature and precipitation changes over a 30 year period around year 60, when the average temperature response is 75% of the estimated temperature response at equilibrium. As both the 1%-per-year and abrupt 4CO2 experiments are available for the IPSL-CM5A-LR and IPSL-CM5A-MR models, we checked that the normalized patterns obtained with the two types of experiment were quite similar, except a slightly larger precipitation change along the ITCZ for the abrupt 4CO2 experiment compare to the 1%-per-year experiment.

For the IPSL-CM5A-LR model, the patterns of temperature and precipitation changes obtained with the 1%-per-year experiment (Fig. 20 and 21) are close to those obtained with the RCP scenarios, confirming that theses patterns are not very sensitive to the scenarios.

The changes simulated by the IPSL-CM4 model (used for CMIP3) and the IPSL-CM5A-LR model are quite different, especially over continents: The normalized temperature increase over the north America, north Asia and in the Arctic region is larger in IPSL-CM4 than in IPSL-CM5A-LR while precipitation changes are significantly different over south America, India, Australia and over the center of the Pacific ocean. Although we have not done dedicated simulations to attribute the origins of these differences, they are consistent with some known modifications. The leaf area index (LAI) was prescribed in CM4 whereas it is computed by the phenology part of the vegetation model (section 2.3) in CM5. Numerical instabilities of the surface temperature which were present in IPSL-CM4 have been now suppressed. The soil depth has been increased as the amount of water that can be stored along the seasons, especially in the tropics. Finally, the change of the horizontal and vertical resolution of the atmospheric model and the tuning process that followed have reduced the biases in the location of the mid-latitude jets and have slightly modified the precipitation over the Pacific ocean (Hourdin et al., this issue-a).

The IPSL-CM5A-LR and IPSL-CM5A-MR models only differ in the horizontal resolution of the atmospheric model, respectively $1.875^o \times 3.75^o$ and $1.25^o \times 2.5^o$ (section 3.2). Both the temperature change and the relative precipitation change display very similar patterns for these two models (Fig. 20 and 21). There are of course some more details when the resolution increases, for instance in the Himalayan region, but there are no significant large scale pattern changes.

The IPSL-CM5A-LR and IPSL-CM5B-LR models only differ in the physical package of the atmospheric model (section 2.2.1). We have previously seen that the climate sensitivity between these two versions was very different. The differences are also dramatic when looking at their spatial patterns. In the CM5B model, the temperature increase in the Arctic region is extremely large, and this high value is found throughout the whole continental regions of the Northern Hemisphere. In the Pacific ocean, the precipitation changes along the equator are located in the center and in the east of the basin in CM5B, whereas it is much more westward, with a strong double ITCZ signature, in CM5A. There is no longer any signature of the South Pacific Convergence Zone (SPCZ) in the precipitation response of CM5B. Over the tropical continents, the differences in precipitations changes are also large, especially over India, East Africa and South America. All these large differences in the precipitations changes among models contrast with the small differences that are present in the climatology of these different models for current conditions (Hourdin et al., this issue-b). The reasons of these large differences in response to a CO_2 increase will be analyzed in detail and will be presented in forthcoming papers.

[Fig. 20 about here.]

[Fig. 21 about here.]

7 Summary and conclusion

The IPSL-CM5 Earth System Model presented in this paper represents an evolutionary step in the development of a coupled dynamical-physical-biogeochemical global general circulation model aiming at studying the Earth's system and anticipating its evolution under natural and anthropogenic influences. The representation in the model of an interactive carbon cycle, of tropospheric and stratospheric chemistry, and of a comprehensive description of aerosols allows us to address science questions that could not be addressed with the IPSL-CM4 coupled ocean-atmosphere climate model used in CMIP3. This includes the study of carbon-climate feedbacks and the estimate of CO_2 emissions compatible with specific atmospheric concentrations of CO_2 and land-use, the assessment of chemistry-climate interactions, the estimate of the role of different forcings: stratospheric ozone, tropospheric ozone, aerosols other than sulfate, among others. However, an important feature of this model is that is may also be used in a large variety of configurations associated with a range of boundary conditions and with the possibility of switching on or off specific feedbacks in the model (carbon-climate feedbacks, chemistry-climate feedbacks, ocean-atmosphere interactions, etc). During the development process of the model, this possibility as always been considered as a key feature to facilitate the interpretation of the model results. In some configurations, the model may also be used with two different ensembles of atmospheric parameterizations (referred to as CM5A and CM5B) and at different horizontal resolutions (referred to as CM5A-LR and CM5A-MR).

The IPSL-CM5A-LR version of the model has been used to perform most of the numerical experiments proposed by CMIP5 (Taylor et al., 2011), including simulations of the present and past climates (even at the paleoclimatic timescale), climate projections associated with different RCPs scenarios, and multiple idealized experiments aiming at better interpret ESM results and inter-model differences. In particular, the ozone and aerosols radiative forcings used to simulate the evolution of climate both over the historical period and in the future have been derived from components of the IPSL-CM5 plateform rather than from external models. As part of CMIP5, this model has also been used to perform decadal hindcasts and forecasts initialized by a realistic ocean state and to explore the predictability of the climate system at the decadal time scale (Swingedouw et al., this issue).

The evaluation of IPSL-CM5A-LR simulations shows that the model exhibits many biases considered as long-standing systematic biases of coupled ocean-atmosphere models. This includes a warm bias of the ocean surface over regions of equatorial upwelling, the presence of a double ITCZ in the equatorial eastern Pacific, the overestimate of precipitation in regimes of atmospheric subsidence, the underestimate of tropical intra-seasonal variability, and an underestimate of the AMOC. In addition, the model exhibits a substantial and pervasive cold bias (especially at middle latitudes). On the other hand, the pre-industrial control simulation do not exhibit any climate drift, and the model predicts a fairly realistic ENSO variability. For the historical period, the net ocean and land CO_2 flux are fully consistent with recent estimations. Compared to its IPSL-CM4 parent (the IPSL OAGCM used in CMIP3), many aspects of the simulations have been improved, due in part to the increase of the horizontal and vertical resolutions of the model, to the improvement of the land surface model and its coupling with the atmosphere, and to several improvement of the ocean model. However, a further increase of the horizontal resolution of the atmospheric model does not result in significant further improvements except for the location of the extratropical jets. On the other hand, coupled ocean-atmosphere simulations run with an improved atmospheric GCM (IPSL-CM5B) exhibit much more improvements in terms of tropical climatology (less double ITCZ, better cloudiness, etc) and tropical variability (e.g. MJO, ENSO) of the current climate, although the mid-latitude atmospheric circulation and the oceanic circulation needs to be improved.

The IPSL-CM5A-LR ESM has been used to perform climate projections associated with different sets of socio-economic scenarios, including CMIP5 RCPs and CMIP3 SRES. Consistently with other model results, the magnitude of global warming projections strongly depends on the socio-economic scenario considered. Simulations associated with different RCPs suggest that there is potential for an aggressive mitigation policy (RCP 2.6) to limit global warming to about two degrees. However it would require a substantial and fast reduction of CO_2 emissions, with no emission at the end of the 21st century and even negative emissions after that. The emissions refer here to fossil-fuel plus cement production emissions, and do not include land-use emissions. We also found that the behavior of some climate system components may change drastically by the end of the 21st century in the case of a no climate policy scenario (RCP 8.5) : the Arctic ocean would become free of sea ice by about 2070, and the Atlantic Meridional Overturning Circulation would largely collapse because of a oceanic feedback: the northward oceanic salinity transport associated with the AMOC decreases, leading to a decrease in sea surface salinity in the convection sites and a decrease of the AMOC. The magnitude of regional temperature and precipitation changes is found to depend fairly linearly on the magnitude of the projected global warming and thus on the scenario considered. However, the geographical patterns of temperature and precipitation changes turn out to be strikingly similar for the different scenarios. This suggests that a key and critical step towards better anticipating and assessing the regional climate response to different climate policy scenarios will consist in physically understanding, for each model, what controls these robust regional patterns using the wide range of CMIP5 idealized experiments.

Our study also showed that the climate sensitivity and regional climate changes associated with a given scenario may be were greatly different when using different representations of physical processes. The pattern of precipitation changes over continents and the transient climate response are significantly different between IPSL-CM4 and IPSL-CM5A models. The equilibrium climate sensitivity of IPSL-CM5A and IPSL-CM5B are drastically different: 3.9 K and 2.4 K respectively. The reasons for these differences are currently under investigation and will be reported in a future paper.

This study also suggests that the comparison of multi-model CMIP3 and CMIP5 climate projections will be difficult owing to large differences between RCP and SRES scenarios. Nevertheless, we found a close resemblance between climate projections associated with RCP 4.5 and SRES B1 scenarios. This is consistent with the close value of the radiative forcing of greenhouse gases for these two scenarios. Were such a result found based on other models, the comparison of SRES B1 and RCP 4.5 projections might thus help to assess how the spread of model projections has evolved between CMIP3 and CMIP5. However, using the idealized 1%-per-year experiment experiment will probably be an even better way to compare multi-model CMIP3 and CMIP5 climate change response.

Acknowledgements The development of the IPSL coupled model and of its various components has largely benefited from the work of numerous colleagues, post-doctoral scientists, or Ph.D. students. We gratefully acknowledgement their contribution to this community effort, and among them Gillali Abdelaziz, Gaëlle Drouot, Alexandre Durand. The research leading to these results was supported by CNRS, CEA, the INSU-LEFE French Program under the project MissTerre, the European Commission's 7th Framework Programme, under the projects COMBINE (Grant n°226520) and IS-ENES (grant n° 228203). This work was made possible thanks to a dedicated SX9 computer that have been made available by GENCI (Grand Equipement National de Calcul Intensif) at CCRT (Centre de Calcul Recherche et Technologie), allocation 016178.

References

Alexander, M. A., I. Blade, M. Newman, J. R. Lanzante, N. C. Lau, and J. D. Scott, 2002: The atmospheric bridge: The influence of ENSO teleconnections on air-sea interaction over the global oceans. *J. Climate*, **15 (16)**, 2205–2231.

Allen, M. R. and W. J. Ingram, 2002: Constraints on future changes in climate and the hydrologic cycle. *Nature*, **419 (6903)**, 224–232, doi:10.1038/nature01092.

Andrews, T. and P. M. Forster, 2008: CO_2 forcing induces semi-direct effects with consequences for climate feedback interpretations. *Geophys. Res. Lett.*, **35**, L04802, doi:10.1029/2007GL032273.

Arakawa, A. and V. R. Lamb, 1981: A potential enstrophy and energy conserving scheme for the shallow water equations. *Mon. Wea. Rev.*, **109 (1)**, 18–36.

Aumont, O. and L. Bopp, 2006: Globalizing results from ocean in situ iron fertilization studies. *Global Biogeochemical Cycles*, **20 (2)**, GB2017, doi:10.1029/2005GB002591.

Aumont, O., L. Bopp, and M. Schulz, 2008: What does temporal variability in aeolian dust deposition contribute to sea-surface iron and chlorophyll distributions? *Geophys. Res. Lett.*, **35 (7)**, L07607, doi:10.1029/2007GL031131.

Axell, L. B., 2002: Wind-driven internal waves and langmuir circulations in a numerical ocean model of the southern Baltic sea. *J. Geophys. Res.-Oce.*, **107 (C11)**, 3204, doi:10.1029/2001JC000922.

Balkanski, Y., 2011: L'influence des aérosols sur le climat. Thèse d'Habilitation à Diriger des Recherches, Université Versailles Saint Quentin, France.

Balkanski, Y., G. Myhre, M. Gauss, G. Rädel, E. J. Highwood, and K. P. Shine, 2010: Direct radiative effect of aerosols emitted by transport: from road, shipping and aviation. *Atmos. Chem. Phys.*, **10 (10)**, 4477–4489, doi:10.5194/acp-10-4477-2010.

Barnier, B., et al., 2006: Impact of partial steps and momentum advection schemes in a global ocean circulation model at eddy-permitting resolution. *Ocean Dynamics*, **56**, 543–567, doi:10.1007/s10236-006-0082-1.

Beckmann, A. and R. Döscher, 1997: A method for improved representation of dense water spreading over topography in geopotential-coordinate models. *J. Phys. Oceanogr.*, **27 (4)**, 581–591.

Bellenger, H., J.-P. Duvel, M. Lengaigne, and P. Levan, 2009: Impact of organized intraseasonal convective perturbations on the tropical circulation. *Geophys. Res. Lett.*, **36**, L16703, doi:10.1029/2009GL039584.

Blanke, B. and P. Delecluse, 1993: Variability of the tropical Atlantic Ocean simulated by a general circulation model with two different mixed-layer physics. *J. Phys. Oceanogr.*, **23 (7)**, 1363–1388.

Bony, S. and K. A. Emanuel, 2001: A parameterization of the cloudiness associated with cumulus convection; evaluation using TOGA COARE data. *J. Atmos. Sci.*, **58**, 3158–3183.

Boucher, O. and U. Lohmann, 1995: The sulfate-CCN-cloud albedo effect: A sensitivity study with two general circulation models. *Tellus, Ser. B*, **47**, 281–300.

Boucher, O. and M. Pham, 2002: History of sulfate aerosol radiative forcings. *Geophys. Res. Lett.*, **29 (9)**, 1308, doi: 10.1029/2001GL014048.

Braconnot, P., F. Hourdin, S. Bony, J.-L. Dufresne, J.-Y. Grandpeix, and O. Marti, 2007: Impact of different convective cloud schemes on the simulation of the tropical seasonal cycle with a coupled ocean-atmosphere model. *Climate Dynamics*, **29 (5)**, 501–520, doi: 10.1007/s00 382–007–0244–y.

Brohan, P., J. J. Kennedy, I. Harris, S. F. B. Tett, and P. D. Jones, 2006: Uncertainty estimates in regional and global observed temperature changes: A new data set from 1850. *J. Geophys. Res.-Atm.*, **111 (D12)**, D12106, doi: 10.1029/2005JD006548.

Burchard, H. and H. Rennau, 2008: Comparative quantification of physically and numerically induced mixing in ocean models. *Ocean Modelling*, **20 (3)**, 293–311, doi:10.1016/j.ocemod.2007.10.003.

Cadule, P., L. Bopp, and P. Friedlingstein, 2009: A revised estimate of the processes contributing to global warming due to climate-carbon feedback. *Geophys. Res. Lett.*, **36**, L14705, doi:10.1029/2009GL038681.

Cassou, C., 2008: Intraseasonal interaction between the Madden-Julian Oscillation and the North Atlantic Oscillation. *Nature*, **455 (7212)**, 523–527, doi:10.1038/nature07286.

Cattiaux, J., B. Quesada, A. Arakelian, F. Codron, R. Vautard, and P. Yiou, ????: .

Clement, A., P. DiNezio, and C. Deser, 2011: Rethinking the Ocean's Role in the Southern Oscillation. *J. Climate*, **24 (15)**, 4056–4072, doi:10.1175/2011JCLI3973.1.

Cleveland, R. B., W. S. Cleveland, J. McRae, and I. Terpenning, 1990: STL: A Seasonal-Trend Decomposition Procedure Based on Loess. *Journal of Official Statistics*, **6 (1)**, 3–73.

Collatz, G., M. Ribas-Carbo, and J. Berry, 1992: Coupled photosynthesis-stomatal conductance model for leaves of C_4 plants. *Aust. J. Plant Physiol*, **19**, 519–538.

Cravatte, S., G. Madec, T. Izumo, C. Menkes, and A. Bozec, 2007: Progress in the 3-D circulation of the eastern equatorial Pacific in a climate ocean model. *Ocean Modelling*, **17 (1)**, 28 – 48, doi:10.1016/j.ocemod.2006.11.003.

de Rosnay, P. and J. Polcher, 1998: Modelling root water uptake in a complex land surface scheme coupled to a GCM. *Hydrol. Earth Syst. Sci.*, **2 (2-3)**, 239–255, doi:10.5194/hess-2-239-1998.

de Rosnay, P., J. Polcher, K. Laval, and M. Sabre, 2003: Integrated parameterization of irrigation in the land surface model ORCHIDEE. Validation over Indian Peninsula. *Geophys. Res. Lett.*, **30 (19)**, 1986, doi:10.1029/2003GL018024.

Déandreis, C., 2008: Impact des aérosols anthropiques sur le climat présent et futur. Thèse, Université Pierre et Marie Curie.

Déandreis, C., Y. Balkanski, J. L. Dufresne, and A. Cozic, 2011: Radiative forcing estimates in coupled climate-chemistry models with emphasis on the role of the temporal variability. *Atmos. Chem. Phys. Discuss.*, **11 (8)**, 24 313–24 364, doi:10.5194/acpd-11-24313-2011.

d'Orgeval, T., J. Polcher, and P. de Rosnay, 2008: Sensitivity of the West African hydrological cycle in ORCHIDEE to infiltration processes. *Hydrol. Earth Syst. Sci.*, **12 (6)**, 1387–1401, doi:10.5194/hess-12-1387-2008.

Ducoudré, N., K. Laval, and A. Perrier, 1993: SECHIBA, a new set of parameterizations of the hydrologic exchanges at the land-atmosphere interface within the LMD atmospheric general circulation model. *Climate Dynamics*, **6**, 248–273.

Dufresne, J.-L. and S. Bony, 2008: An assessment of the primary sources of spread of global warming estimates from coupled atmosphere-ocean models. *J. Climate*, **21 (19)**, 5135–5144, doi:10.1175/2008JCLI2239.1.

Dufresne, J.-L., J. Quaas, O. Boucher, F. Denvil, and L. Fairhead, 2005: Contrasts in the effects on climate of anthropogenic sulfate aerosols between the 20^{th} and the 21^{st} century. *Geophys. Res. Lett.*, **32**, L21 703, doi:10.1029/2005GL023 619.

Duvel, J. P., H. Bellenger, G. Bellon, and M. Remaud, this issue: An event-by-event assessment of tropical intraseasonal perturbations for general circulation models. *Submitted to Climate Dynamics*.

Emanuel, K. A., 1991: A scheme for representing cumulus convection in large-scale models. *J. Atmos. Sci.*, **48**, 2313–2335.

Emile-Geay, J. and G. Madec, 2009: Geothermal heating, diapycnal mixing and the abyssal circulation. *Ocean Science*, **5 (2)**, 203–217.

Escudier, R., J. Mignot, and D. Swingedouw, this issue: A 20-yrs coupled ocean-sea ice-atmosphere variablility mode in the North Atlantic in an AOGCM. *Submitted to Climate Dynamics*.

Eyring, V., et al., 2010a: Multi-model assessment of stratospheric ozone return dates and ozone recovery in CCMVal-2 models. *Atmos. Chem. Phys.*, **10 (19)**, 9451–9472, doi:10.5194/acp-10-9451-2010.

Eyring, V., et al., 2010b: Sensitivity of 21st century stratospheric ozone to greenhouse gas scenarios. *Geophys. Res. Lett.*, **37**, L16807, doi:10.1029/2010GL044443.

Farquhar, G., S. von Caemmener, and J. Berry, 1980: A biochemical model of photosynthesis CO_2 fixation in leaves of C_3 species. *Planta*, **49**, 78–90.

Fichefet, T. and M. A. Morales Maqueda, 1997: Sensitivity of a global sea ice model to the treatment of ice thermodynamics and dynamics. *J. Geophys. Res.*, **102 (C6)**, 12,609–12,646, doi:10.1029/97JC00480.

Fichefet, T. and M. A. Morales Maqueda, 1999: Modelling the influence of snow accumulation and snow-ice formation on the seasonal cycle of the Antarctic sea-ice cover. *Climate Dynamics*, **15 (4)**, 251–268, doi:10.1007/s003820050280.

Folberth, G. A., D. A. Hauglustaine, J. Lathiere, and F. Brocheton, 2006: Interactive chemistry in the Laboratoire de Meteorologie Dynamique general circulation model: model description and impact analysis of biogenic hydrocarbons on tropospheric chemistry. *Atmos. Chem. Phys.*, **6**, 2273–2319, doi:10.5194/acp-6-2273-2006.

Forster, P., et al., 2007: Changes in atmospheric constituents and in radiative forcing. *Climate Change 2007: The Scientific Basis. Contribution of Working Group I to the Fourth Assessment Report of the Intergovernmental Panel on Climate Change*, S. Solomon, D. Qin, M. Manning, Z. Chen, M. Marquis, K. B. Averyt, M. Tignor, and H. L. Miller, Eds., Cambridge University Press, Cambridge, United Kingdom and New York, NY, USA, chap. 2, 129–234.

Fouquart, Y. and B. Bonnel, 1980: Computations of solar heating of the Earth's atmosphere: A new parametrization. *Contrib. Atmos. Phys.*, **53**, 35–62.

Friedlingstein, P., et al., 2006: Climate-carbon cycle feedback analysis: Results from the C4MIP model intercomparison. *J. Climate*, **19 (14)**, 3337–3353, doi:10.1175/JCLI3800.1.

Fröhlich, C. and J. Lean, 2004: Solar radiative output and its variability: evidence and mechanisms. *Astron. Astrophys. Rev.*, **12 (4)**, 273–320, doi:10.1007/s00159-004-0024-1.

Gent, P. R. and J. C. Mcwilliams, 1990: Isopycnal mixing in ocean circulation models. *J. Phys. Oceanogr.*, **20 (1)**, 150–155.

Goulet, L. and J. P. Duvel, 2000: A new approach to detect and characterize intermittent atmospheric oscillations: Application to the intraseasonal oscillation. *J. Atmos. Sci.*, **57 (15)**, 2397–2416, doi:10.1175/1520-0469(2000)057¡2397:ANATDA¿2.0.CO;2.

Grandpeix, J.-Y. and J.-P. Lafore, 2010: A Density Current Parameterization Coupled with Emanuel's Convection Scheme. Part I: The Models. *J. Atmos. Sci.*, **67 (4)**, 881–897, doi:10.1175/2009JAS3045.1.

Grandpeix, J.-Y., J.-P. Lafore, and F. Cheruy, 2010: A Density Current Parameterization Coupled with Emanuel's Convection Scheme. Part II: 1D Simulations. *J. Atmos. Sci.*, **67 (4)**, 898–922, doi:10.1175/2009JAS3045.1.

Gregory, J. and M. Webb, 2008: Tropospheric adjustment induces a cloud component in CO_2 forcing. *J. Climate*, **21 (1)**, 58–71, doi:10.1175/2007JCLI1834.1.

Gregory, J. M., et al., 2004: A new method for diagnosing radiative forcing and climate sensitivity. *Geophys. Res. Lett.*, **31 (3)**, L03205, doi:10.1029/2003GL018747.

Guemas, V. and F. Codron, 2011: Differing impacts of resolution changes in latitude and longitude on the mid-latitudes in the LMDZ GCM. *J. Climate*, **in press**, doi:10.1175/2011JCLI4093.1.

Guilyardi, E., A. Wittenberg, A. Fedorov, M. Collins, C. Wang, A. Capotondi, G. J. van Oldenborgh, and T. Stockdale, 2009: Understanding El Nino in ocean-atmosphere general circulation models: progress and challenges. *Bull. Am. Meteorol. Soc.*, **90 (3)**, 325–340, doi:10.1175/2008BAMS2387.1.

Hall, A., 2004: The role of surface albedo feedback in climate. *J. Climate*, **17 (7)**, 1550–1568.

Hansen, J., et al., 2005: Efficacy of climate forcings. *J. Geophys. Res.-Atm.*, **110 (D18)**, D18104, doi: 10.1029/2005JD005776.

Hauglustaine, D., F. Hourdin, L. Jourdain, M. Filiberti, S. Walters, J. Lamarque, and E. Holland, 2004: Interactive chemistry in the Laboratoire de Meteorologie Dynamique general circulation model: Description and background tropospheric chemistry evaluation. *J. Geophys. Res.-Atm.*, **109 (D4)**, D04314, doi:10.1029/2003JD003957.

Held, I. M. and B. J. Soden, 2006: Robust responses of the hydrological cycle to global warming. *J. Climate*, **19**, 56865699.

Hibler, W. D., 1979: A dynamic thermodynamic sea ice model. *J. Phys. Oceanogr.*, **9 (4)**, 815–846.

Hourdin, F. and A. Armengaud, 1999: The use of finite-volume methods for atmospheric advection of trace species. part i: Test of vairious formulations in a general circulation model. *Mon. Wea. Rev.*, **127**, 822–837.

Hourdin, F., F. Couvreux, and L. Menut, 2002: Parameterisation of the dry convective boundary layer based on a mass flux representation of thermals. *J. Atmos. Sci.*, **59**, 1105–1123.

Hourdin, F., et al., 2006: The LMDZ4 general circulation model: climate performance and sensitivity to parametrized physics with emphasis on tropical convection. *Climate Dynamics*, **27 (7-8)**, 787–813, doi: 10.1007/s00 382–006–0158–0.

Hourdin, F., et al., this issue-a: From LMDZ4 to LMDZ5 : impact of the atmospheric model grid configuration on the climate and sensitivity of IPSL climate model. *Submited to Climate Dynamics*.

Hourdin, F., et al., this issue-b: From LMDZ5A to LMDZ5B : revisiting the parameterizations of clouds and convection in the atmosperic component of the IPSL-CM5 climate model. *Submited to Climate Dynamics*.

Huffman, G., R. Adler, M. Morrissey, D. Bolvin, S. Curtis, R. Joyce, B. McGavock, and J. Susskind, 2001: Global precipitation at one-degree daily resolution from multisatellite observations. *J. Hydrometeor.*, **2 (1)**, 36–50.

Hurtt, G., et al., 2011: Harmonization of land-use scenarios for the period 1500-2100: 600 years of global gridded annual land-use transitions, wood harvest, and resulting secondary lands. *Climatic Change*, **109**, 117–161, 10.1007/s10584-011-0153-2.

IPCC, 2007: *Climate Change 2007: The Scientific Basis. Contribution of Working Group I to the Fourth Assessment Report of the Intergovernmental Panel on Climate Change*, S. Solomon, D. Qin, M. Manning, Z. Chen, M. Marquis, K. B. Averyt, M. Tignor, and H. L. Miller, Eds., Cambridge University Press, Cambridge, United Kingdom and New York, NY, USA, 996.

Jam, A., F. Hourdin, C. Rio, and F. Couvreux, 2011: Resolved versus parametrized boundary-layer plumes. Part III: A diagnostic boundary-layer cloud parameterization derived from large eddy simulations. *Boundary-Layer Meteorol.*, **submitted**.

Johns, T., et al., 2011: Climate change under aggressive mitigation: The ENSEMBLES multi-model experiment. *Climate Dynamics*, **37 (8-10)**, 1975–2003, doi:10.1007/s00382-011-1005-5.

Jones, P. D., M. New, D. E. Parker, S. Martin, and I. G. Rigor, 1999: Surface air temperature and its changes over the past 150 years. *Rev. Geophys.*, **37 (2)**, 173–199, doi:10.1029/1999RG900002.

Jourdain, L., S. Bekki, F. Lott, and F. Lefevre, 2008: The coupled chemistry-climate model LMDz-REPROBUS: description and evaluation of a transient simulation of the period 1980-1999. *Annales Geophysicae*, **26 (6)**, 1391–1413, doi:10.5194/angeo-26-1391-2008.

Kamala, K., Y. Peings, P. Terray, and H. Douville, this issue: ENSO-Indian monsoon teleconnection in the CNRM and IPSL historical simulations. *Submitted to Climate Dynamics*.

Kim, S. T. and F.-F. Jin, 2011: An ENSO stability analysis. Part II: results from the twentieth and twenty-first century simulations of the CMIP3 models. *Climate Dynamics*, **36 (7-8)**, 1609–1627, doi:10.1007/s00382-010-0872-5.

Klein Goldewijk, K., A. Beusen, G. van Drecht, and M. de Vos, 2011: The hyde 3.1 spatially explicit database of human-induced global land-use change over the past 12,000 years. *Global Ecology and Biogeography*, **20 (1)**, 73–86, doi:10.1111/j.1466-8238.2010.00587.x.

Koch-Larrouy, A., M. Lengaigne, P. Terray, G. Madec, and S. Masson, 2010: Tidal mixing in the Indonesian Seas and its effect on the tropical climate system. *Climate Dynamics*, **34 (6)**, 891–904, doi:10.1007/s00382-009-0642-4.

Koch-Larrouy, A., G. Madec, P. Bouruet-Aubertot, T. Gerkema, L. Bessieres, and R. Molcard, 2007: On the transformation of Pacific Water into Indonesian Throughflow Water by internal tidal mixing. *Geophys. Res. Lett.*, **34 (4)**, L04604, doi:10.1029/2006GL028405.

Konsta, D., H. Chepfer, J.-L. Dufresne, A. Idelkadi, and G. Cesana, this issue: Evaluation of clouds simulated by the LMDZ5 GCM using A-train satellite observations (CALIPSO-PARASOL-CERES). *Submitted to Climate Dynamics*.

Krinner, G., et al., 2005: A dynamic global vegetation model for studies of the coupled atmosphere-biosphere system. *Global Biogeochemical Cycles*, **19 (1)**, GB1015, doi:10.1029/2003GB002199.

Lamarque, J.-F., G. Kyle, M. Meinshausen, K. Riahi, S. Smith, D. van Vuuren, A. Conley, and F. Vitt, 2011: Global and regional evolution of short-lived radiatively-active gases and aerosols in the representative concentration pathways. *Climatic Change*, **109 (1-2)**, 191–212, doi:10.1007/s10584-011-0155-0.

Lamarque, J.-F., et al., 2010: Historical (1850-2000) gridded anthropogenic and biomass burning emissions of reactive gases and aerosols: methodology and application. *Atmos. Chem. Phys.*, **10 (15)**, 7017–7039, doi:10.5194/acp-10-7017-2010.

Large, W. and S. Yeager, 2009: The global climatology of an interannually varying air-sea flux data set. *Climate Dynamics*, **33**, 341–364, doi:10.1007/s00382-008-0441-3.

Lathière, J., D. Hauglustaine, N. de Noblet-Ducoudré, G. Krinner, and G. A. Folberth, 2005: Past and future changes in biogenic volatile organic compound emissions simulated with a global dynamic vegetation model. *Geophys. Res. Lett.*, **32**, L20818, doi:10.1029/2005GL024164.

Laval, K., R. Sadourny, and Y. Serafini, 1981: Land surface processes in a simplified general circulation model. *Geophys. Astrophys. Fluid Dyn.*, **17**, 129–150.

Le Quéré, C., et al., 2009: Trends in the sources and sinks of carbon dioxide. *Nature Geoscience*, **2 (12)**, 831–836, doi:10.1038/ngeo689.

Le Sommer, J., T. Penduff, S. Theetten, G. Madec, and B. Barnier, 2009: How momentum advection schemes influence current-topography interactions at eddy permitting resolution. *Ocean Modelling*, **29 (1)**, 1–14, doi:10.1016/j.ocemod.2008.11.007.

Lean, J., 2009: Calculations of solar irradiance: monthly means from 1882 to 2008, annual means from 1610 to 2008. http://www.geo.fu-berlin.de/en/met/ag/strat/forschung/SOLARIS/Input_data/-Calculations_of_Solar_Irradiance.pdf.

Lean, J., G. Rottman, J. Harder, and G. Kopp, 2005: SORCE contributions to new understanding of global change and solar variability. *Solar Phys.*, **230**, 27–53, doi:10.1007/s11207-005-1527-2.

Lefevre, F., G. P. Brasseur, I. Folkins, A. K. Smith, and P. Simon, 1994: Chemistry of the 1991-1992 stratospheric winter: Three-dimensional model simulations. *J. Geophys. Res.-Atm.*, **99 (D4)**, 8183–8195, doi:10.1029/93JD03476.

Lefevre, F., F. Figarol, K. S. Carslaw, and T. Peter, 1998: The 1997 Arctic ozone depletion quantified from three-dimensional model simulations. *Geophys. Res. Lett.*, **25 (13)**, 2425–2428, doi:10.1029/98GL51812.

Lengaigne, M., G. Madec, L. Bopp, C. Menkes, O. Aumont, and P. Cadule, 2009: Bio-physical feedbacks in the Arctic Ocean using an Earth system model. *Geophys. Res. Lett.*, **36**, L21602, doi:10.1029/2009GL040145.

Lengaigne, M., C. Menkes, O. Aumont, T. Gorgues, L. Bopp, J.-M. Andre, and G. Madec, 2007: Influence of the oceanic biology on the tropical Pacific climate in a coupled general circulation model. *Climate Dynamics*, **28 (5)**, 503–516, doi:10.1007/s00382-006-0200-2.

Lenton, A., F. Codron, L. Bopp, N. Metzl, P. Cadule, A. Tagliabue, and J. L. Sommer, 2009: Stratospheric ozone depletion reduces ocean carbon uptake and enhances ocean acidification. *Geophys. Res. Lett.*, **36**, L12606, doi:10.1029/2009GL038227.

Liebmann, B. and C. A. Smith, 1996: Description of a complete (interpolated) outgoing longwave radiation dataset. *Bull. Am. Meteorol. Soc.*, **77 (6)**, 1275–1277.

Lloyd, J., E. Guilyardi, and H. Weller, 2011a: The role of atmosphere feedbacks during ENSO in the CMIP3 models. Part II: using AMIP runs to understand the heat flux feedback mechanisms. *Climate Dynamics*, **37 (7-8)**, 1271–1292, doi:10.1007/s00382-010-0895-y.

Lloyd, J., E. Guilyardi, and H. Weller, 2011b: The role of atmosphere feedbacks during ENSO in the CMIP3 models. Part III: The shortwave flux feedback. *Submitted to J. Climate*.

Lott, F., 1999: Alleviation of Stationary Biases in a GCM through a Mountain Drag Parameterization Scheme and a Simple Representation of Mountain Lift Forces. *Mon. Wea. Rev.*, **127**, 788–801.

Lott, F., L. Fairhead, F. Hourdin, and P. Levan, 2005: The stratospheric version of LMDz: dynamical climatologies, arctic oscillation, and impact on the surface climate. *Climate Dynamics*, **25 (7-8)**, 851–868, doi:10.1007/s00382-005-0064-x.

Louis, J.-F., 1979: A parametric model of vertical eddy fluxes in the atmosphere. *Boundary-Layer Meteorol.*, **17**, 187–202.

Loveland, T. R., B. C. Reed, J. F. Brown, D. O. Ohlen, Z. Zhu, L. Yang, and J. W. Merchant, 2000: Development of a global land cover characteristics database and IGBP DISCover from 1 km AVHRR data. *Int. J. Remote Sens.*, **21 (6-7)**, 1303–1330, doi:10.1080/014311600210191, `http://www.tandfonline.com/doi/pdf/10.1080/014311600210191`.

Ludwig, W., J. Probst, and S. Kempe, 1996: Predicting the oceanic input of organic carbon by continental erosion. *Global Biogeochemical Cycles*, **10 (1)**, 23–41, doi:10.1029/95GB02925.

Lévy, M., A. Estublier, and G. Madec, 2001: Choice of an advection scheme for biogeochemical models. *Geophys. Res. Lett.*, **28 (19)**, 3725–3728, doi:10.1029/2001GL012947.

Madec, G., 2008: NEMO ocean engine. Technical note, IPSL. Available at http://www.nemo-ocean.eu/content/download/15482/73217/file/NEMO_book_v3_3.pdf.

Madec, G. and M. Imbard, 1996: A global ocean mesh to overcome the North Pole singularity. *Climate Dynamics*, **12 (6)**, 381–388, doi:10.1007/BF00211684.

Madronich, S. and S. Flocke, 1998: The role of solar radiation in atmospheric chemistry. *Handbook of Environmental Chemistry*, P. Boule, Ed., Springer-Verlag, Heidelberg, 1–26.

Manabe, S. and R. J. Stouffer, 1980: Sensitivity of a global climate model to an increase of CO_2 concentration in the atmosphere. *J. Geophys. Res.-Oce.*, **85 (C10)**, 5529–5554, doi:10.1029/JC085iC10p05529.

Marti, O., et al., 2010: Key features of the IPSL ocean atmosphere model and its sensitivity to atmospheric resolution. *Climate Dynamics*, **34**, 1–26, doi:10.1007/s00382-009-0640-6.

Maury, P., F. Lott, L. Guez, and J.-P. Duvel, this issue: Tropical variability and stratospheric equatorial waves in the IPSLCM5 model. *Submitted to Climate Dynamics*.

Meehl, G. A., C. Covey, T. Delworth, M. Latif, B. McAvaney, J. F. B. Mitchell, and R. J. Stouffer, 2007a: The WCRP CMIP3 multi-model dataset: A new era in climate change research. *Bull. Am. Meteorol. Soc.*, **88 (9)**, 1383–1394, doi:10.1175/BAMS-88-9-1383.

Meehl, G. A., C. Covey, B. McAvaney, M. Latif, and R. J. Stouffer, 2005: Overview of the Coupled Model Intercomparison Project. *Bull. Am. Meteorol. Soc.*, **86 (1)**, 89–93.

Meehl, G. A., et al., 2007b: Global climate projections. *Climate Change 2007: The Scientific Basis. Contribution of Working Group I to the Fourth Assessment Report of the Intergovernmental Panel on Climate Change*, S. Solomon, D. Qin, M. Manning, Z. Chen, M. Marquis, K. B. Averyt, M. Tignor, and H. L. Miller, Eds., Cambridge University Press, Cambridge, United Kingdom and New York, NY, USA, chap. 10, 747–846.

Meinshausen, M., et al., 2011: The RCP greenhouse gas concentrations and their extension from 1765 to 2300. *Climatic Change*, **109**, 213–241, doi:10.1007/s10584-011-0156-z.

Mellor, G. and A. Blumberg, 2004: Wave breaking and ocean surface layer thermal response. *J. Phys. Oceanogr.*, **34 (3)**, 693–698, doi:10.1175/2517.1.

Menut, L., O. P.Tripathi, A. Colette, R. Vautard, E. Flaounas, and B. Bessagnet, this issue: Evaluation of regional climate simulations for air quality modelling purposes. *Submitted to Climate Dynamics*.

Merryfield, W. J., G. Holloway, and A. E. Gargett, 1999: A global ocean model with double-diffusive mixing. *J. Phys. Oceanogr.*, **29 (6)**, 1124–1142.

Morcrette, J.-J., L. Smith, and Y. Fouquart, 1986: Pressure and temperature dependence of the absorption in longwave radiation parametrizations. *Contrib. Atmos. Phys.*, **59 (4)**, 455–469.

Morgenstern, O., et al., 2010: Review of the formulation of present-generation stratospheric chemistry-climate models and associated external forcings. *J. Geophys. Res.-Atm.*, **115**, D00M02, doi:10.1029/2009JD013728.

Morissey, M. L., 1990: An evaluation of ship data in the equatorial western Pacific. *J. Climate*, **3 (1)**, 99–112.

Moss, R. H., et al., 2010: The next generation of scenarios for climate change research and assessment. *Nature*, **463 (7282)**, 747–756, doi:10.1038/nature08823.

Najjar, R. G., et al., 2007: Impact of circulation on export production, dissolved organic matter, and dissolved oxygen in the ocean: Results from Phase II of the Ocean Carbon-cycle Model Intercomparison Project (OCMIP-2). *Global Biogeochemical Cycles*, **21 (3)**, GB3007, doi:10.1029/2006GB002857.

Pham, M., O. Boucher, and D. Hauglustaine, 2005: Changes in atmospheric sulfur burdens and concentrations and resulting radiative forcings under IPCC SRES emission scenarios for 1990-2100. *J. Geophys. Res.-Atm.*, **110**, D06112, doi:10.1029/2004JD005125.

Piao, S., P. Ciais, P. Friedlingstein, N. de Noblet-Ducoudre, P. Cadule, N. Viovy, and T. Wang, 2009: Spatiotemporal patterns of terrestrial carbon cycle during the 20th century. *Global Biogeochemical Cycles*, **23**, GB4026, doi: 10.1029/2008GB003339.

Quaas, J. and O. Boucher, 2005: Constraining the first aerosol indirect radiative forcing in the LMDZ GCM using POLDER and MODIS satellite data. *Geophys. Res. Lett.*, **32**, L17814, doi:10.1029/2005GL023850.

Ramaswamy, V., et al., 2001: Radiative forcing of climate change. *Climate Change 2001: The Scientific Basis. Contribution of Working Group I to the Third Assessment Report of the Intergovernmental Panel on Climate Change*, J. T. Houghton, Y. Ding, D. J. Griggs, M. Noguer, P. J. van der Linden, X. Dai, K. Maskell, and C. A. Johnson, Eds., Cambridge University Press, Cambridge, United Kingdom and New York, NY, USA, chap. 6, 349–416.

Rayner, N. A., D. E. Parker, E. B. Horton, C. K. Folland, L. V. Alexander, D. P. Rowell, E. C. Kent, and A. Kaplan, 2003: Global analyses of sea surface temperature, sea ice, and night marine air temperature since the late nineteenth century. *J. Geophys. Res.-Atm.*, **108 (D14)**, 4407, doi:10.1029/2002JD002670.

Rio, C. and F. Hourdin, 2008: A thermal plume model for the convective boundary layer : Representation of cumulus clouds. *J. Atmos. Sci.*, **65**, 407–425.

Rio, C., F. Hourdin, F. Couvreux, and A. Jam, 2010: Resolved Versus Parametrized Boundary-Layer Plumes. Part II: Continuous Formulations of Mixing Rates for Mass-Flux Schemes. *Boundary-Layer Meteorol.*, **135**, 469–483, doi: 10.1007/s10546-010-9478-z.

Sadourny, R. and K. Laval, 1984: January and July performance of the LMD General Circulation Model. *New Perspectives in Climate Modelling*, Elsevier Science Publishers, Amsterdam, 173–198.

Sander, S. P., et al., 2006: Chemical kinetics and photochemical data for use in atmospheric studies, evaluation no. 15. JPL Publication 06-2, Jet Propulsion Laboratory, Pasadena (CA), USA. URL `http://jpldataeval.jpl.nasa.gov`.

Sato, M., J. E. Hansen, M. P. McCormick, and J. B. Pollack, 1993: Stratospheric aerosol optical depths, 1850-1990. *J. Geophys. Res.-Atm.*, **98 (D12)**, 22 987–22 994, doi:10.1029/93JD02553.

Schulz, M., 2007: Constraining model estimates of the aerosol radiative forcing. Thèse d'Habilitation à Diriger des Recherches, Université Pierre et Marie Curie, Paris, France.

Schulz, M., Y. Balkanski, W. Guelle, and F. Dulac, 1998: Role of aerosol size distribution and source location in a three-dimensional simulation of a saharan dust episode tested against satellite-derived optical thickness. *J. Geophys. Res.-Atm.*, **103 (D9)**, 10 579–10 592, doi:10.1029/97JD02779.

Simmons, H. L., S. R. Jayne, L. C. S. Laurent, and A. J. Weaver, 2004: Tidally driven mixing in a numerical model of the ocean general circulation. *Ocean Modelling*, **6 (3-4)**, 245–263, doi:10.1016/S1463-5003(03)00011-8.

Sitch, S., et al., 2003: Evaluation of ecosystem dynamics, plant geography and terrestrial carbon cycling in the LPJ dynamic global vegetation model. *Global Change Biology*, **9**, 161–185, doi:10.1046/j.1365-2486.2003.00569.x.

Son, S. W., et al., 2010: Impact of stratospheric ozone on Southern Hemisphere circulation change: A multimodel assessment. *J. Geophys. Res.-Atm.*, **115**, D00M07, doi:10.1029/2010JD014271.

SPARC, 2010: SPARC report on the evaluation of chemistry-climate models, V. Eyring and T. G. Shepherd and D. W. Waugh (Eds.). SPARC Report No. 5, WCRP-132, WMO/TD-No. 1526, http://www.atmosp.physics.utoronto.ca/SPARC.

Stommel, H., 1961: Thermohaline convection with two stable regimes of flow. *Tellus*, **13 (2)**, 224–230, doi:10.1111/j.2153-3490.1961.tb00079.x.

Swingedouw, D., P. Braconnot, P. Delecluse, E. Guilyardi, and O. Marti, 2007a: The impact of global freshwater forcing on the thermohaline circulation: adjustment of North Atlantic convection sites in a CGCM. *Climate Dynamics*, **28 (2)**, 291–305, doi:10.1007/s00382-006-0171-3.

Swingedouw, D., P. Braconnot, P. Delecluse, E. Guilyardi, and O. Marti, 2007b: Quantifying the AMOC feedbacks during a 2xCO2 stabilization experiment with land-ice melting. *Climate Dynamics*, **29 (5)**, 521–534, doi:10.1007/s00382-007-0250-0.

Swingedouw, D., J. Mignot, S. Labetoule, E. Guilyardi, and G. Madec, this issue: Initialisation and predictability of the AMOC over the last 50 years in a climate model. *Submitted to Climate Dynamics*.

Szopa, S., et al., this issue: Aerosol and ozone changes as forcing for climate evolution between 1850 and 2100. *Submitted to Climate Dynamics*.

Takahashi, K., 2009: Radiative constraints on the hydrological cycle in an idealized radiative-convective equilibrium model. *J. Atmos. Sci.*, **66 (1)**, 77–91, doi:10.1175/2008JAS2797.1.

Taylor, K. E., R. J. Stouffer, and G. A. Meehl, 2011: An overview of CMIP5 and the experiment design. *Bull. Am. Meteorol. Soc.*, doi:10.1175/BAMS-D-11-00094.1.

Terray, P., 2011: Southern Hemisphere extra-tropical forcing: a new paradigm for El Niño-Southern Oscillation. *Climate Dynamics*, **36 (11-12)**, 2171–2199, doi:10.1007/s00382-010-0825-z.

Tiedtke, M., 1989: A comprehensive mass flux scheme for cumulus parameterization in large-scale models. *Mon. Wea. Rev.*, **117**, 1179–1800.

Valcke, S., 2006: OASIS3 User's Guide (prism-2-5). Tech. Rep. TR/CMGC/06/73, PRISM Report No 3, CERFACS, Toulouse, France.

Van Leer, B., 1977: Towards the ultimate conservative difference scheme : IV. A new approach to numerical convection. *J. Computational Phys.*, **23**, 276–299.

van Vuuren, D., et al., 2011: The representative concentration pathways: an overview. *Climatic Change*, 1–27, 10.1007/s10584-011-0148-z.

Vial, T. J., J.and Osborn, this issue: Relationship between sudden stratospheric warming and tropospheric blocking as simulated by the multi-century IPSL-CM5A coupled climate model. *Submitted to Climate Dynamics*.

Wang, Y. M., J. L. Lean, and N. R. Sheeley, 2005: Modeling the sun's magnetic field and irradiance since 1713. *Astrophys. J.*, **625 (1)**, 522–538, doi:10.1086/429689.

Wanninkhof, R., 1992: Relationship between wind-speed and gas-exchange over the ocean. *J. Geophys. Res.-Oce.*, **97 (C5)**, 7373–7382, doi:10.1029/92JC00188.

Wittenberg, A. T., 2009: Are historical records sufficient to constrain ENSO simulations? *Geophys. Res. Lett.*, **36**, doi:10.1029/2009GL038710.

WMO, 2011: Scientific Assessment of Ozone Depletion: 2010. Global Ozone Research and Monitoring Project, Report N°52, World Meteorological Organization, http://www.unep.ch/ozone/Assessment_Panels/SAP/-Scientific_Assessment_2010/index.shtml.

Xavier, P. K., J.-P. Duvel, P. Braconnot, and F. J. Doblas-Reyes, 2010: An Evaluation Metric for Intraseasonal Variability and its Application to CMIP3 Twentieth-Century Simulations. *J. Climate*, **23 (13)**, 3497–3508, doi: 10.1175/2010JCLI3260a.1.

List of Figures

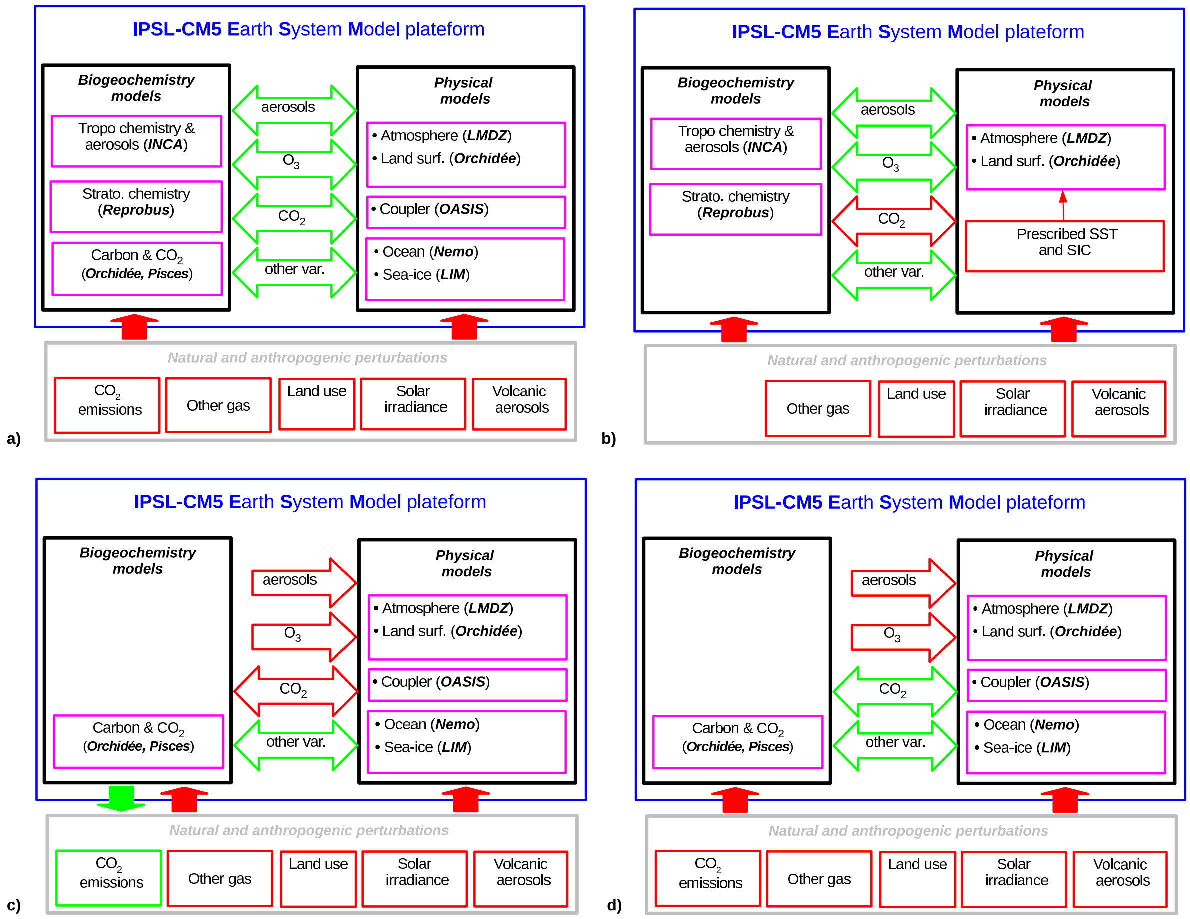

Fig. 1: Schematic of the IPSL-CM5 ESM platform. The individual models that constitute the platform are in violet boxes, the variables that are computed are in green boxes and those that are prescribed in red boxes. In **a)**, the "plain configuration" is shown, with all the models being active. In **b)**, the "atmospheric chemistry configuration" is shown, where the ocean and the carbon cycle models have been replaced by prescribed boundary conditions : ocean surface temperature, sea-ice fraction and CO_2 concentration. In **c)**, the "climate-carbon configuration" is shown, where the chemistry and aerosol models have been replaced by prescribed conditions (ozone and aerosols 3D fields). The CO_2 concentration is prescribed and the "implied CO_2 emissions" are computed. In **d)**, the same configuration as in **c)** is shown, except that CO_2 emissions are prescribed and CO_2 concentration is computed.

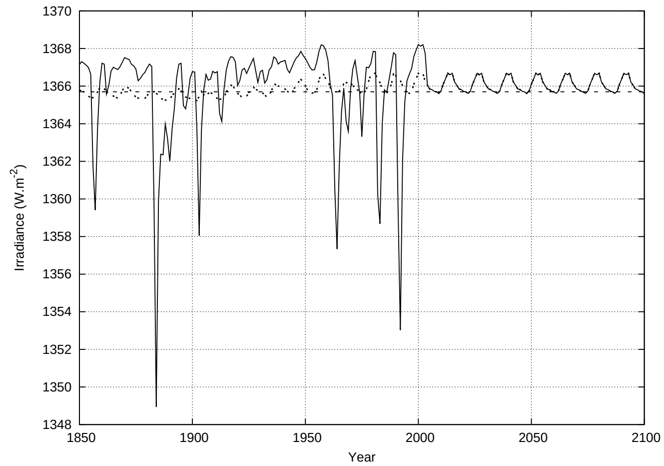

Fig. 2: Time evolution of the total solar irradiance with (solid line) and without (dotted line) volcanic euptions. Also reported is the reference value used for all the runs except the historical and the scenario runs (dashed line).

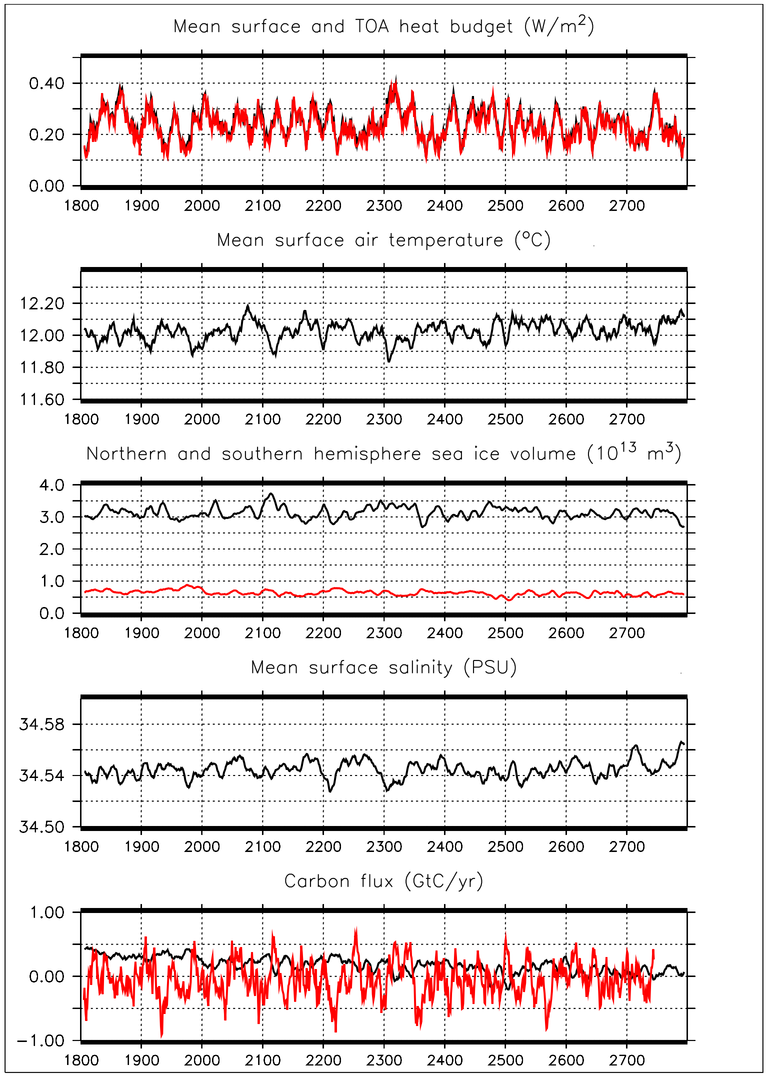

Fig. 3: The ime evolution of (a) the global mean heat budget at surface and at the TOA (b) the global mean air surface temperature (c) the sea-ice volume in the northern (black) and southern (red) hemisphere, (d) the global mean surface salinity and (e) carbon flux (PgC/yr) over ocean (black) and over land (red), for the 1000 years first of the control run. The data are smoothed using a 11 years Hanning filter.

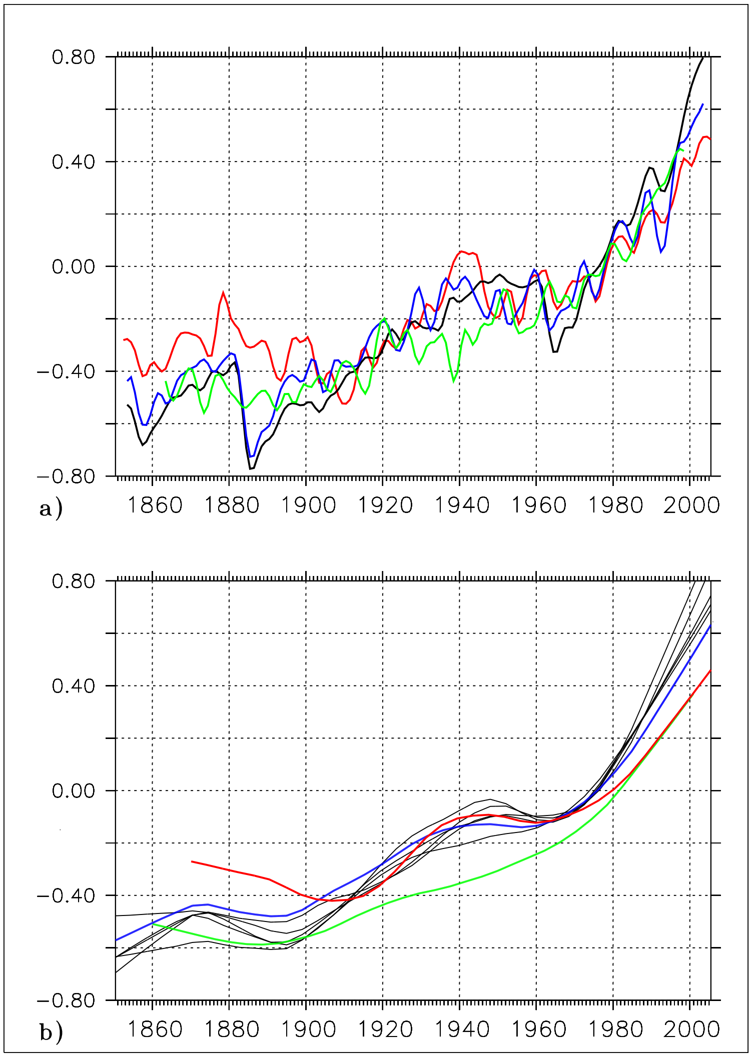

Fig. 4: **(a)** Time evolution of the global mean air surface temperature observed (Hadcrut3v dataset, red), simulated by the IPSL-CM5A-LR (black), IPSL-CM5A-MR (blue) and IPSL-CM4 (green) models. The temperature are smoothed using a 5 years Hanning filter **(b)** Trends of the same variables, the trends being estimated from the global area-averaged temperature anomalies monthly time series (from the base period 1961-90) with the help of the STL (Seasonal-Trend decomposition procedure based on Loess). The unit is ^{o}C. Note that for IPSL-CM5A-LR, 5 members are available; in (a) the averaged value of these members are shown (for clarity) whereas in (b) the trends have been estimated separately on each simulation member and each of these trends is shown.

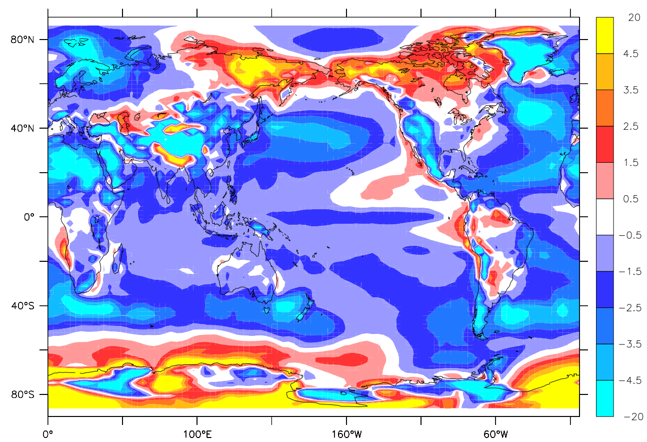

(a)

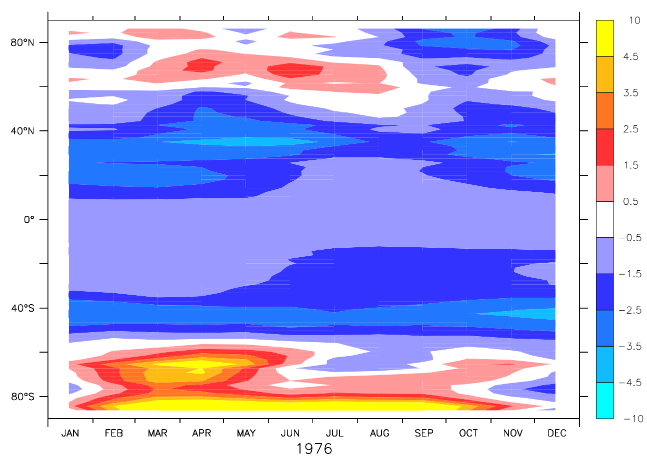

(b)

Fig. 5: Bias in the climatology (period 1961-1990) of the air surface temperature compared to CRU estimate (Jones et al., 1999) (a) annual mean (b) zonal average of monthly mean. The unit is ^oC.

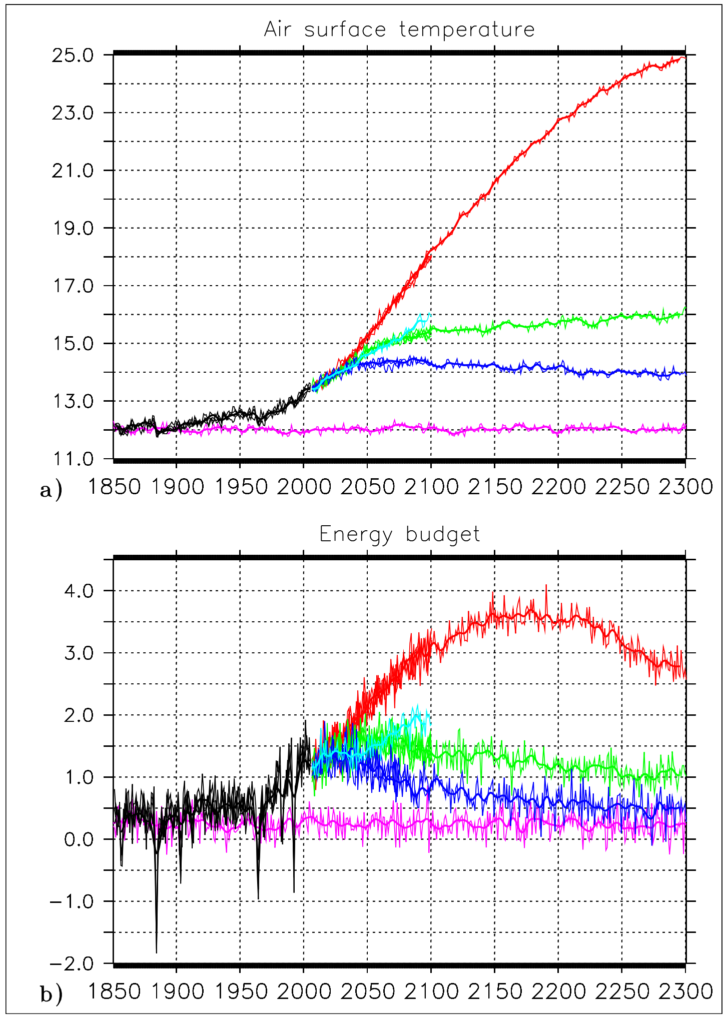

Fig. 6: Time evolution of the global mean air surface temperature **(a)** and the net radiative flux TOA **(b)** for the control run (purple), the historical runs (black), and for the four RCP scenarios: RCP-2.6 (blue), RCP-4.5 (green), RCP-6 (light blue), and RCP-8.5 (red). Thin lines correspond to the annual value of individual run members, thick lines correspond to the 11 years running mean of one particular member. For all the scenarios, one member last until year 2300 except for the RCP-6 scenario for which the only member stop in 2100.

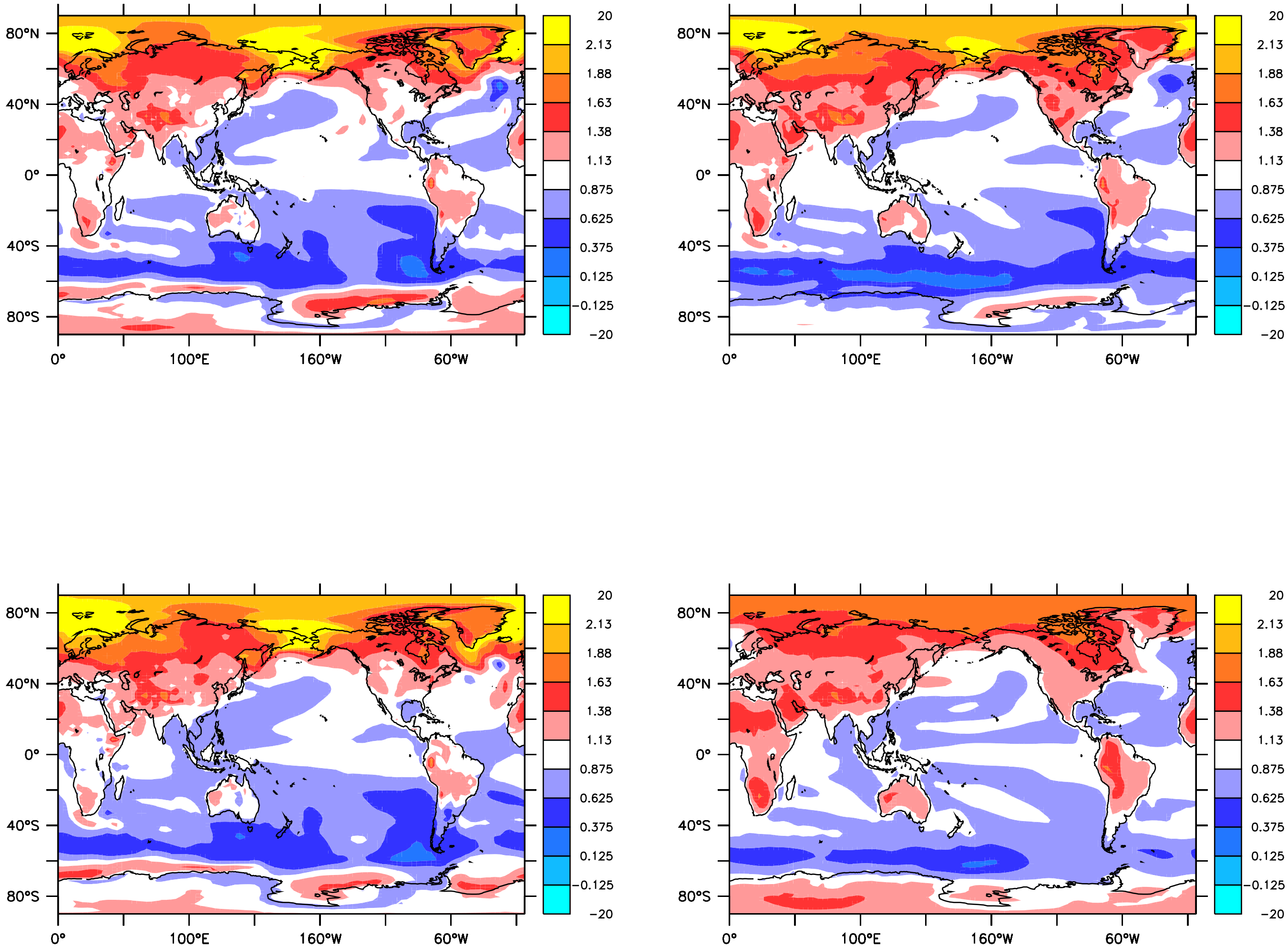

Fig. 7: Geographical distribution of the normalized temperature change for the RCP 2.6 (left column) and the RCP 8.5 (right column) scenarios at the end of the 21st century (2070-2100 period, top row) and at the end of the 23 century (2270-2300 period, bottom row). The temperature change is computed relative to the preindustrial run (100 years average), and the local temperature change is normalized with the global average temperature change.

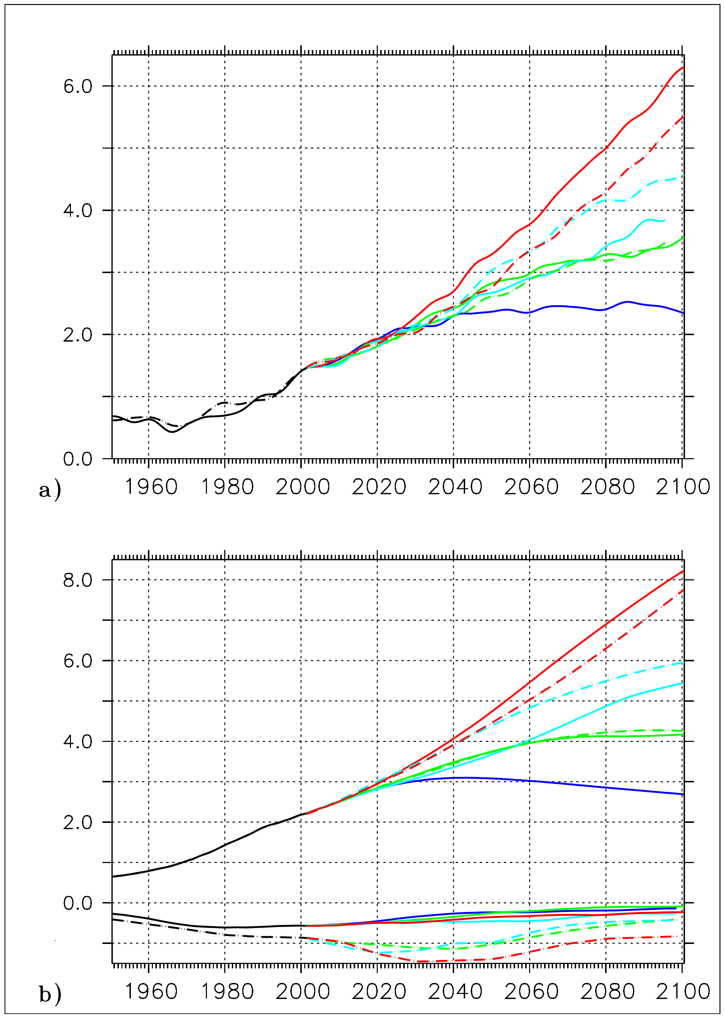

Fig. 8: Time evolution of **(a)** the global mean air surface temperature and of **(b)** the long-lived greenhouse gases (CO_2, CH_4, N_2O, CFC... but no ozone) (positive values) and aerosol (negative values) radiative forcing (direct+first indirect) simulated with IPSL-CM5A-LR for the historical and the futur periode, using the forcing of the RCP (line) and SRES (dash) scenarios. The historical runs are in black. The four RCP scenarios used in CMIP5 are: RCP-2.6 (blue), RCP-4.5 (green), RCP-6 (light blue), and RCP-8.5 (red). The three SRES scenarios used in CMIP3 are: SRES-B1 (green), SRES-A1B (light blue), and SRES-A2 (red)

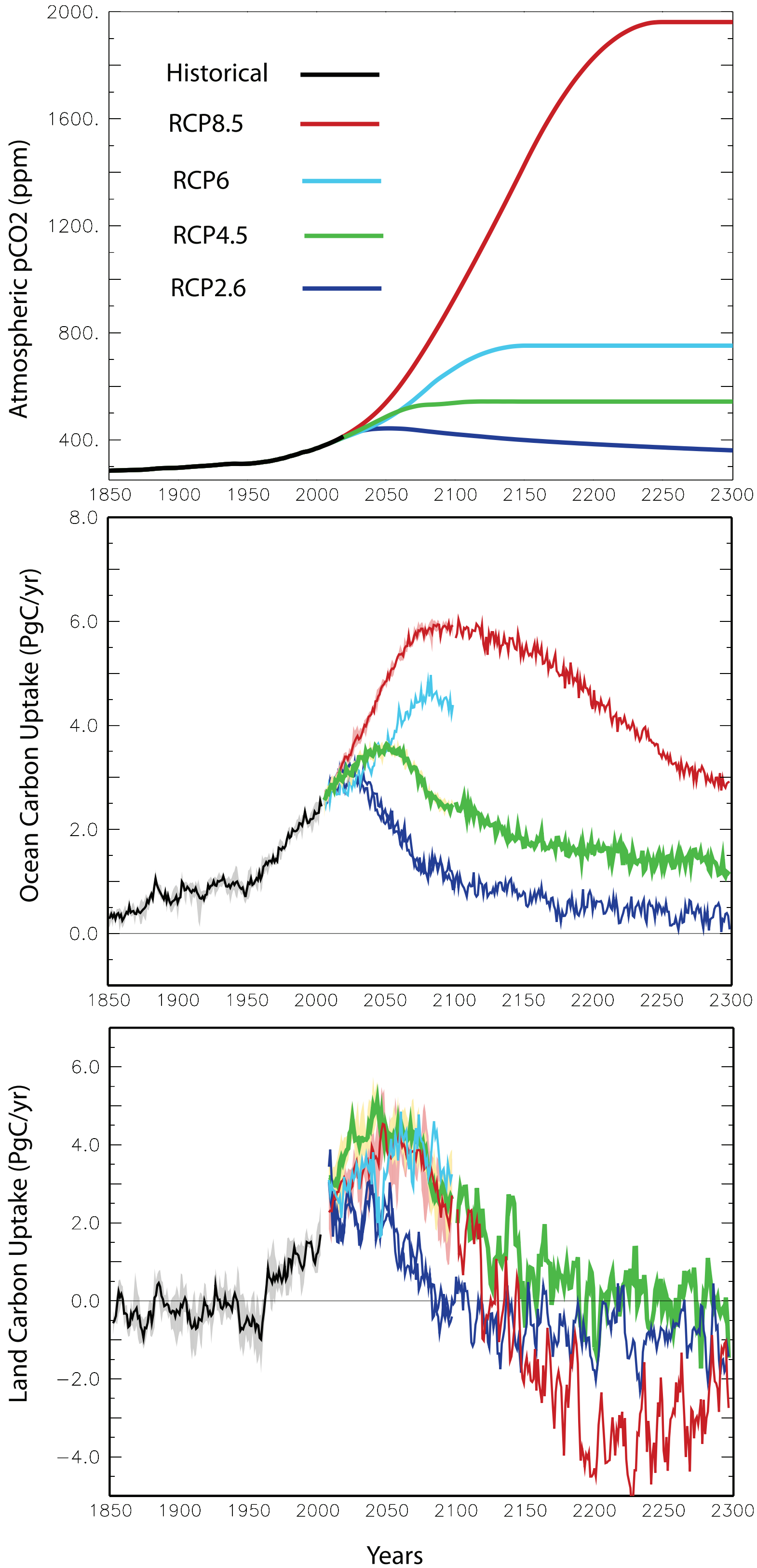

Fig. 9: Time evolution of the prescribed CO_2 concentration (top), the computed ocean carbon uptake (mid) and land carbon uptake (bottom) for the historical period (black) and for the four RCP scenarios: RCP2.6 (blue), RCP 4.5, RCP6.0 and RCP8.5 (red). The concentration is in ppmv and the carbon flux in PgC/yr. Note that the simulated net land carbon flux does include a land-use component (see text).

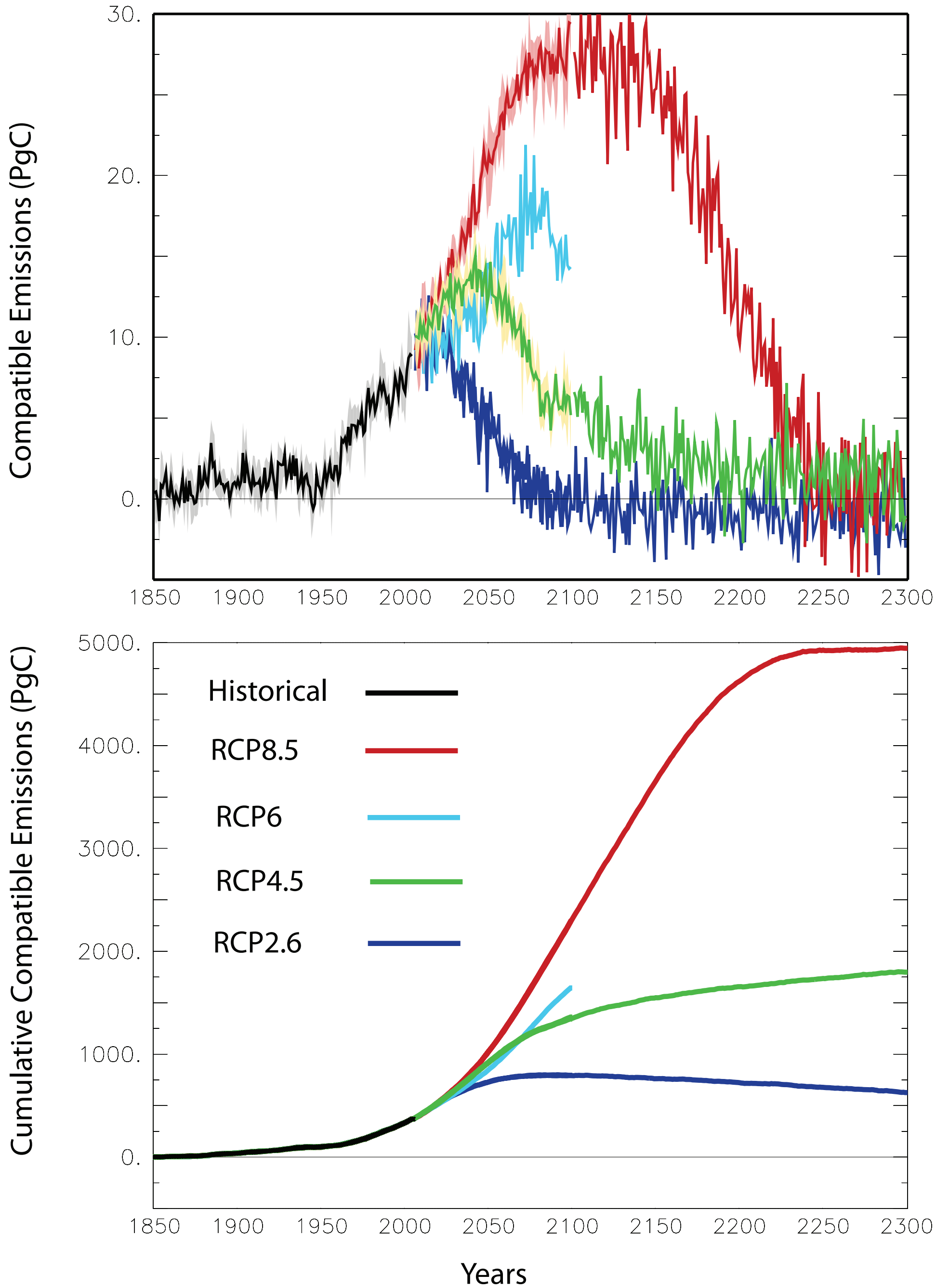

Fig. 10: Time evolution of the compatible CO_2 emissions (top, in PgC/yr) and of the cumulative of these emissions (bottom, in PgC) for the historical period (black) and for the four RCP scenarios: RCP2.6 (blue), RCP 4.5, RCP6.0 and RCP8.5 (red). The compatible emissions refer here to fossil-fuel + cement production only emissions, and do not include lan-use emissions.

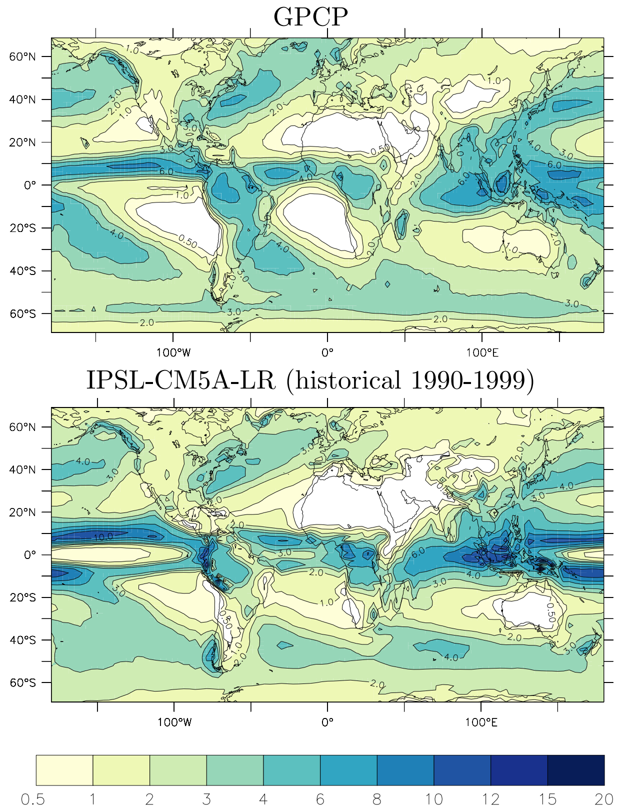

Fig. 11: 10-year annual mean rainfall (mm/day) in the GPCP observations and the IPSL-CM5A-LR model for the period 1990-1999.

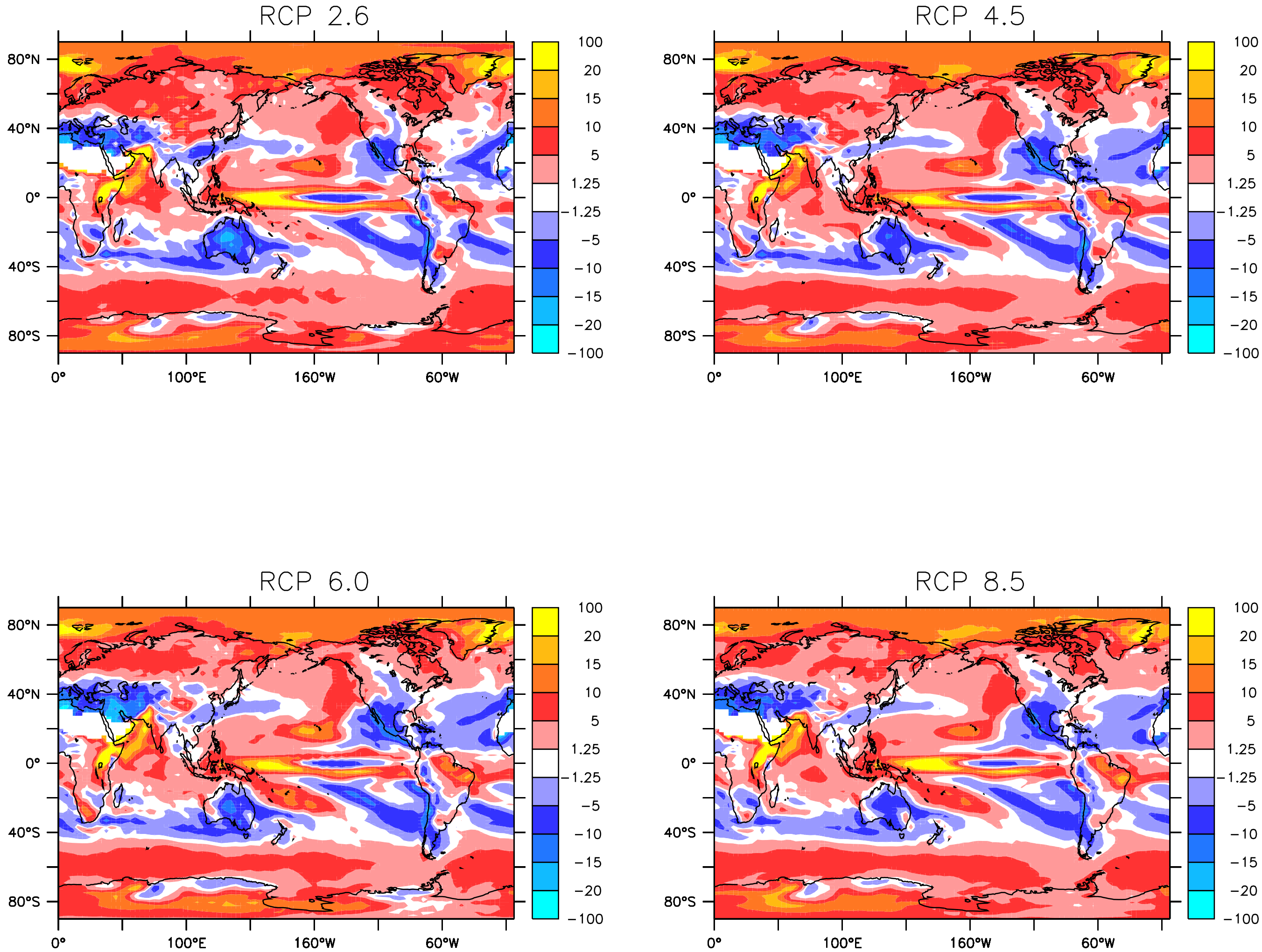

Fig. 12: Geographical distribution of the normalized relative precipitation changes for the four RCP scenarios at the end of the 21st century (units are %/K). The local precipitation changes are computed relative to their local preindustrial values on a yearly mean basis and are then normalized with the global average temperature change. The regions where the annual mean temperature is less then 0.01 mm/day (i.e. the Sahara region) are left blank.

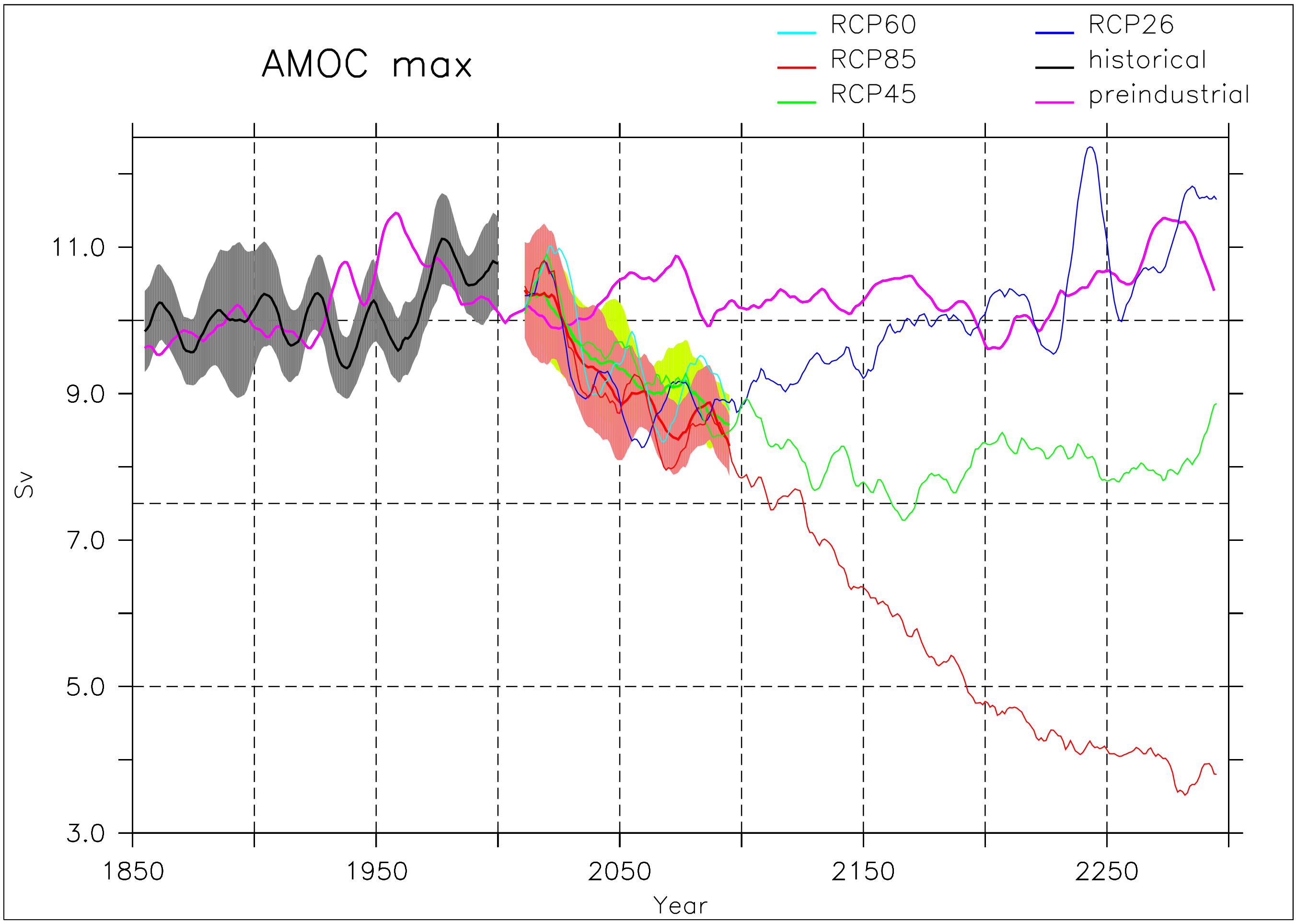

Fig. 13: Atlantic Meridional Overturning Circulation (AMOC) maximum taken between 500 m to the bottom and from 30°S to 80°N. In purple is the control run; in black is the historical ensemble mean, with a two standard deviation overlap in gray; in red is the RCP85 ensemble mean, with a two standard deviation overlap in light red; in green is the RCP45 ensemble mean, with a two standard deviation overlap in light green. In blue is RCP26 simulation and in light blue a RCP60 simulation.

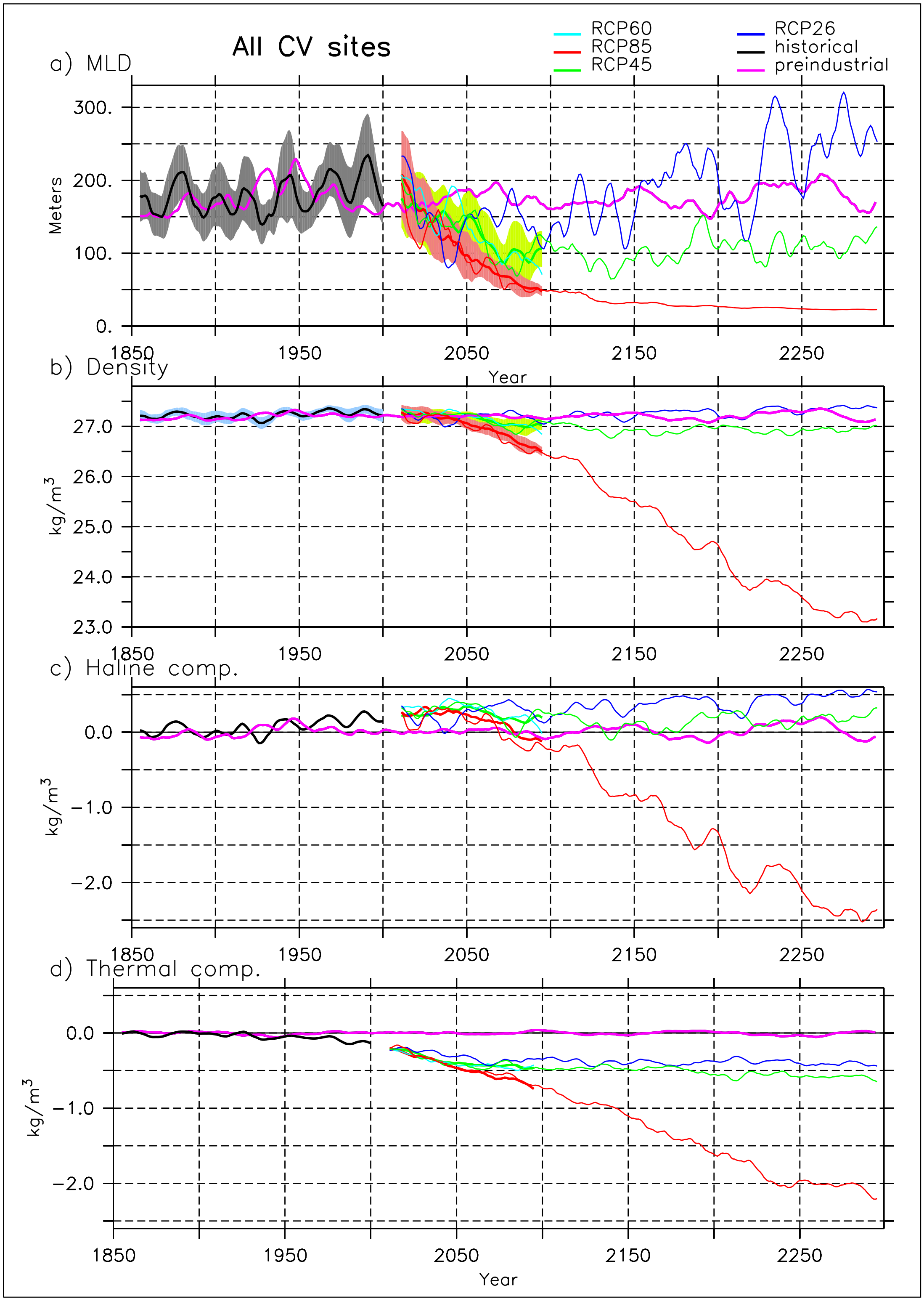

Fig. 14: Similar figure as Fig. 13 but for a) the mixed layer depth (MLD) in meters for winter season (DJFM) averaged other the convection sites (definition in Escudier et al. (this issue), b) surface density averaged over the same region (in kg/m3), c) decomposition in haline components (related to salinity) of the linearized surface density (in kg/m3), d) thermal components (related to temperature) of the same linearization.

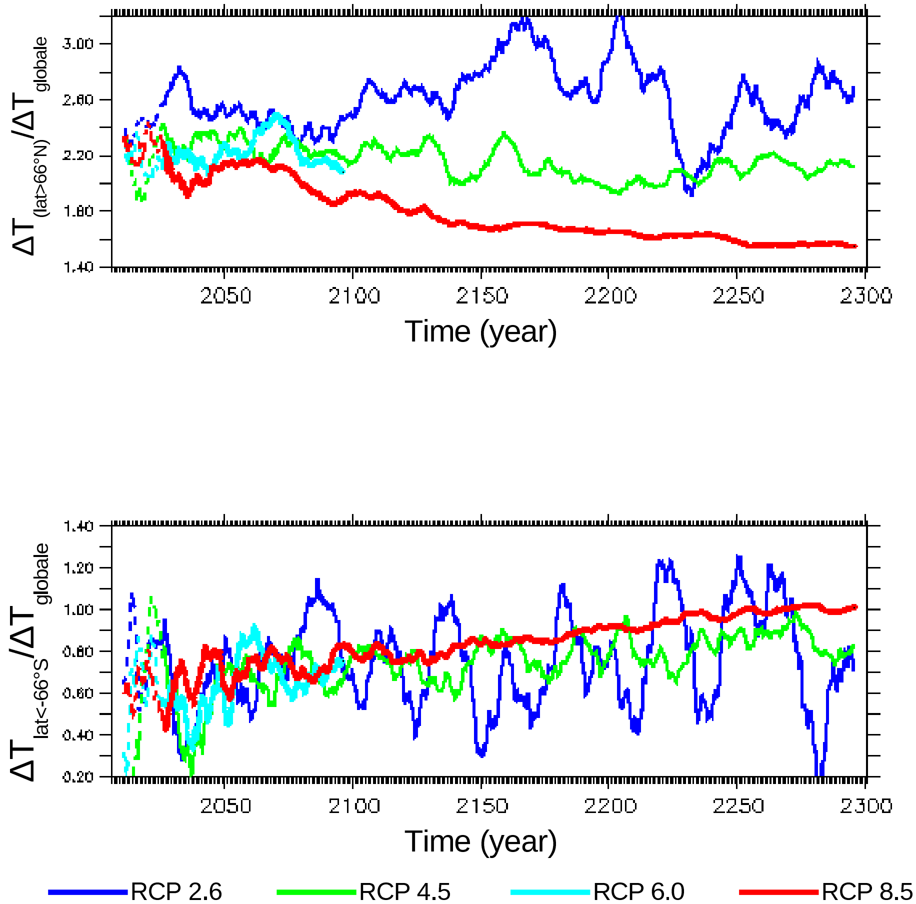

Fig. 15: Time evolution of polar amplification for both hemisphere, poleward of the arctic (top) and antarctic (bottom) circles, for the four RCP scenarios. The polar amplification is computed every month and plotted with a 10 years running average. The simulation ends in 2100 for the RCP6.0 scenario. The temperature increase is computed relative to the preindustrial run.

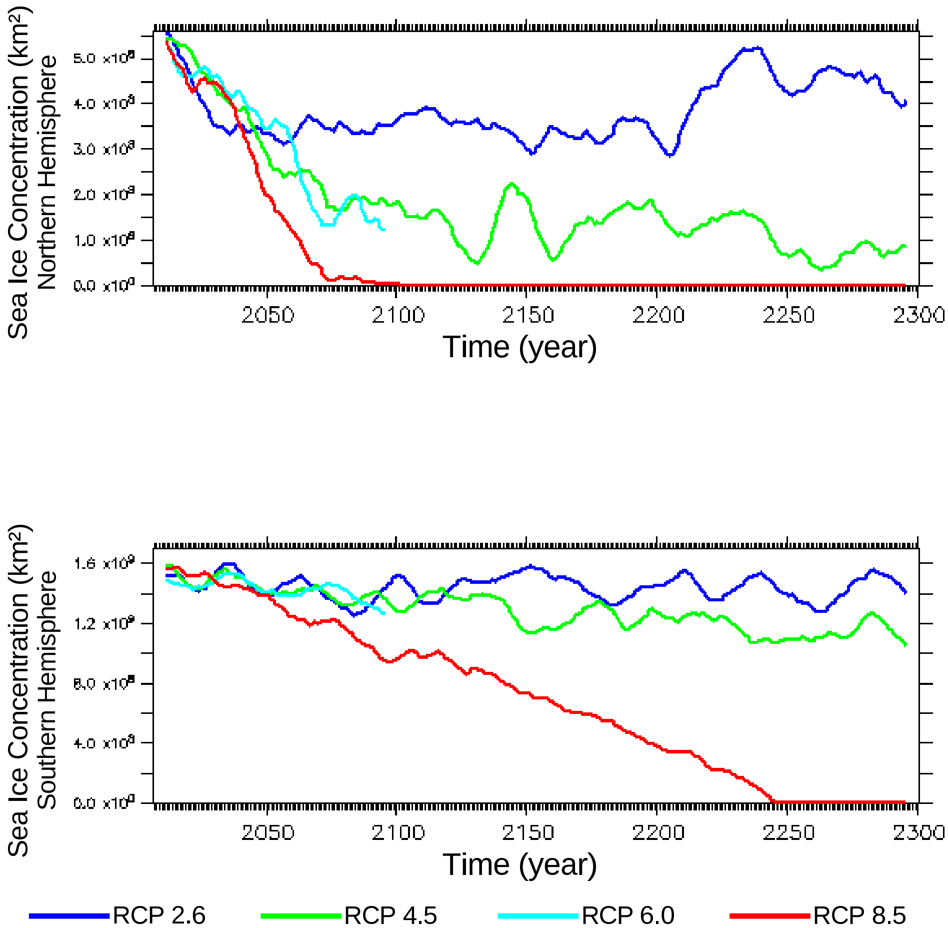

Fig. 16: Time evolution of the sea ice extent (km^2) in September, for the four RCP scenarios and for both hemisphere: north (top) and south (bottom). A 10 years running average is applied.

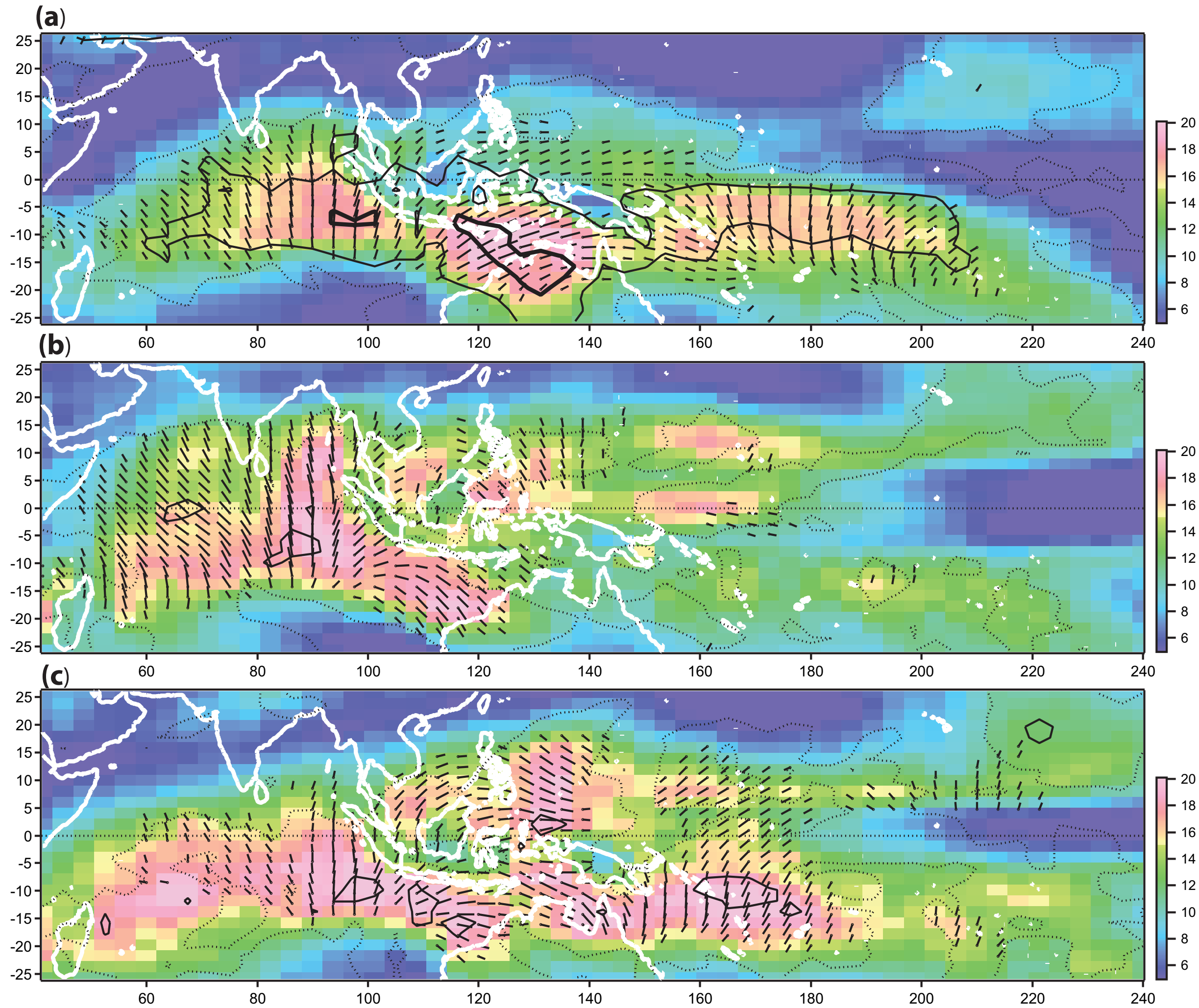

Fig. 17: Average amplitude of LMA intraseasonal events (colors), JFM average event (ticks, the local amplitude is the length and the relative phase is the angle) and (contours)average percentage of local intraseasonal variance that is due to large scale organized perturbation (dotted: 40%; thin: 50% and bold: 60%) for (a) NOAA OLR, (b) IPSL-CM5A-LR and (c) IPSL-CM5B-LR. The relative phases for one average event show the propagation of the event: When one follows the direction of propagation, the ticks turn clockwise (for example on Fig. 17-a going to the East at 10°S from 60°E to 180°E the ticks turn clockwise indicating an eastward propagation).

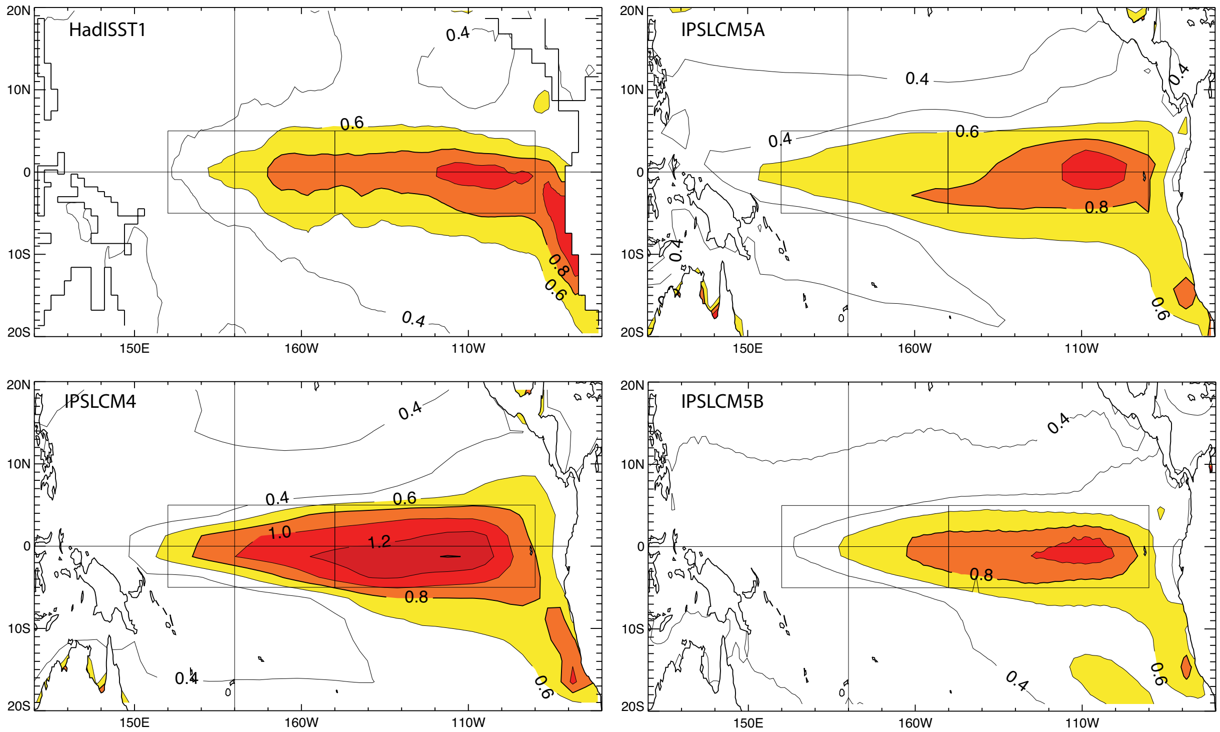

Fig. 18: Standard deviations (K) of monthly SST anomalies with respect to the mean seasonal cycle for HadISST1 (1870-2008) (Rayner et al., 2003) and for 200 years of IPSL-CM5A-LR and IPSL-CM4.

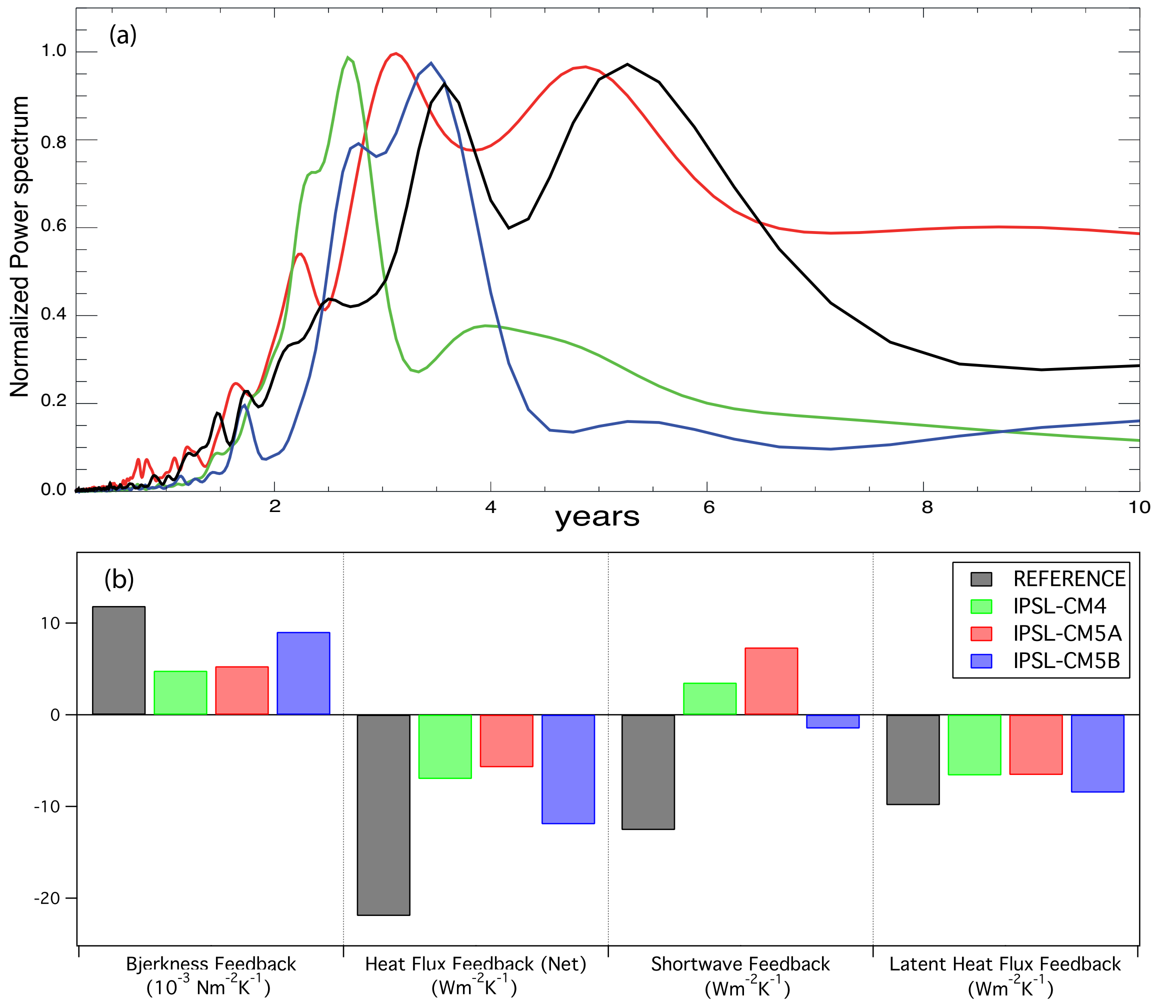

Fig. 19: (a) Normalized power spectra of SST over Niño3 for (black) HadISST1, (green), IPSL-CM4, (red) IPSL-CM5A-LR and (blue) IPSL-CM5B-LR. (b) The evaluation of the Bjerkness and the heat flux feedbacks. The two main components of the latter: the shortwave and latent heat flux feedbacks are also reported. For the feedback coefficients, the reference is ERA40 (1958-2001).

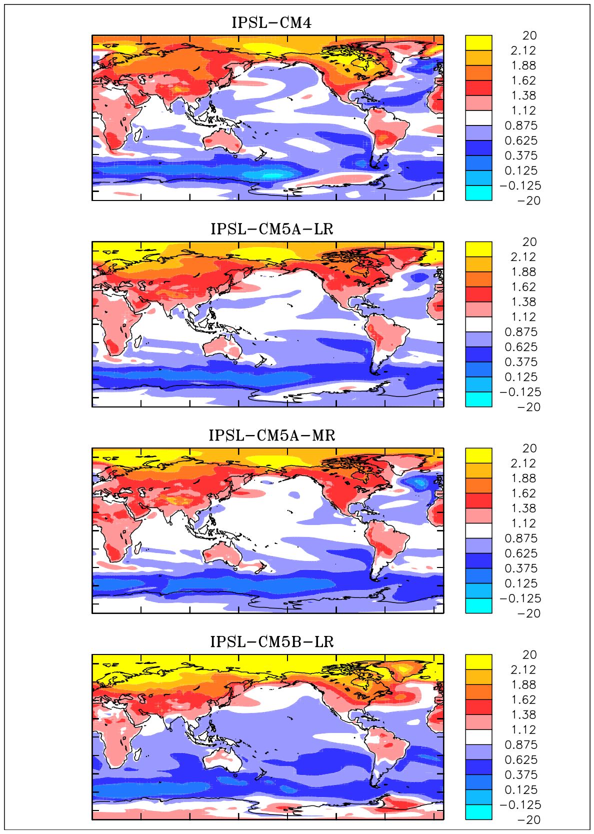

Fig. 20: Geographical distribution of the normalized temperature change simulated by four versions of the IPSL-CM model in response to a increase of the concentration of CO_2. The temperature change is computed relative to the preindustrial control run, and the local temperature change is normalized with the global average temperature change.

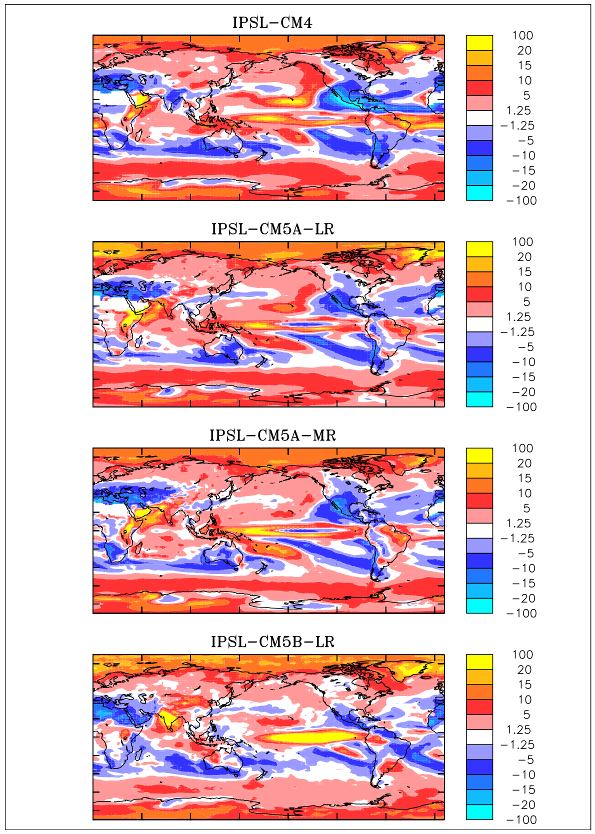

Fig. 21: Same as Fig. 20 but for the normalized relative precipitation changes (units are %/K). The local precipitation changes are computed relative to their local preindustrial values on a yearly mean basis and are then normalized with the global average temperature change. The regions where the annual mean temperature is less then 0.01 mm/day (i.e. the Sahara region) are left blank.

List of Tables

model	1%/year CO_2 increase				abrupt $4xCO_2$		
	$\Delta Q_t(2CO_2)$	λ	$\Delta T_s^t(2CO_2)$	$\Delta T_s^e(2CO_2)$	$\Delta Q_t(2CO_2)$	λ	$\Delta T_s^e(2CO_2)$
	(Wm^{-2})	($Wm^{-2}K^{-1}$)	(K)	(K)	(Wm^{-2})	($Wm^{-2}K^{-1}$)	(K)
IPSL-CM4	3.5	-0.98	1.8	3.6			
IPSL-CM5A-LR	3.5	-1.04	2.1	3.4	3.3	-0.85	3.9
IPSL-CM5A-MR	3.5	-1.05	2.1	3.4			
IPSL-CM5B-LR					3.1	-1.3	2.4

Table 1: Radiative forcing for a doubling of CO_2 $\Delta Q_t(2CO_2)$, feedback parameter λ, transient $\Delta T_s^t(2CO_2)$ and equilibrium $\Delta T_s^e(2CO_2)$ air surface temperature increase in response to a CO_2 doubling for different version of the IPSL-CM model. These values (except the transient temperature response) are estimated using either the 1%/year CO_2 increase experiment or the abrupt $4CO_2$ experiment.